Table 1 Composition of titanium powder (mass%).

Fe	Si	Mn	Mg	C	Cl	N	O	H	Ti
0.03	0.01	<0.01	<0.001	0.01	<0.002	0.01	0.25	0.04	Bal.

(values by the manufacturer)

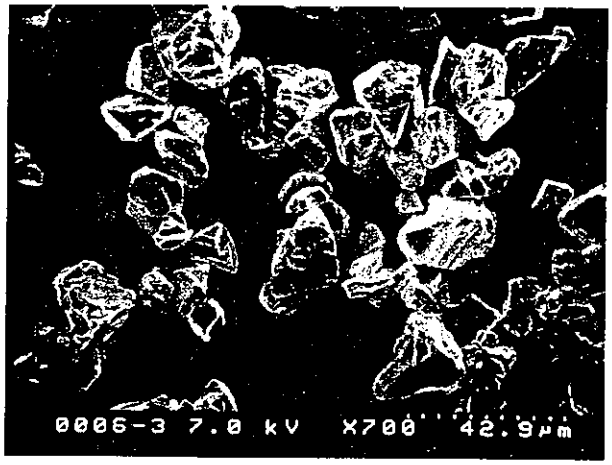

Fig. 1 SEM image of titanium powder used.

physical and mechanical properties of the titanium castings sintered without the mold.

2. Materials and Methods

2.1 Titanium powder

Commercial titanium powder (TC-459, Toho Tiatnium Co. Ltd., Tokyo, Japan) produced by the hydride/dehydride process[19] was used. The particle size was less than 16μm. The composition is shown in Table 1, and the SEM image of the powder is shown Fig. 1.

2.2 Plaster molds

Two kinds of split plaster molds used in this study are shown in Fig. 2. These were produced by pouring a mixture of plaster and water (water/plaster = 0.7) into the negative form of metal mold. The split plaster molds were separated from the metal mold after the mixture had set and were then

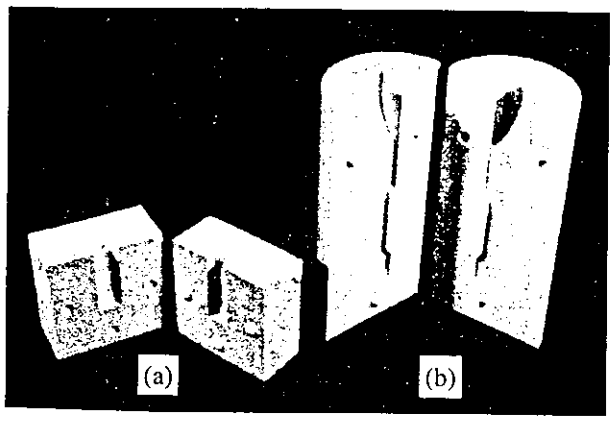

Fig. 2 Gypsum molds. (a) cylindrical casting, (b) dumbbell-type casting.

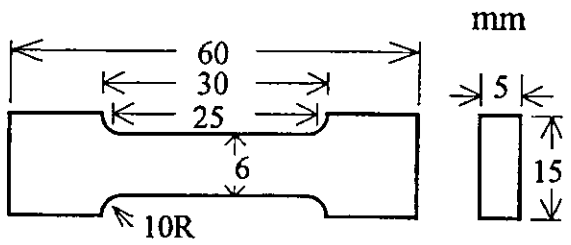

Fig. 3 Sizes of a dumbbell-type casting.

Table 2 Compositions of slips (mass%).

Slip	W/P	Titanium powder	Water	Sodium alginate
I	0.391	71.59	28.03	0.38
II	0.354	73.59	26.03	0.38
III	0.318	75.59	24.03	0.38

dried in an oven at 318 K for 172.8 ks. One mold, used for a cylindrical casting, had a cavity of 10 mm in diameter and 30 mm in length, and the other mold had a dumbbell-type space and reservoir. Sizes of the dumbbell-type casting for tensile tests are shown in Fig. 3.

2.3 Viscosities of slips

The compositions of three slips with different water-powder ratio (W/P) are shown in Table 2. The slips were prepared by mixing titanium powder, water and sodium alginate (chemical regent grade, viscosity at 1 w/v% and 293 K: 0.3–0.4 Pa·s; Wako Pure Chemical Industry, Ltd., Osaka, Japan) in a vessel with a motor-mixer for 0.9 ks, followed by evacuation to remove air bubbles in the slips. Minimum viscosity of each slip was examined with a rotation viscosimeter (BL-type, Tokyo Keiki Co. Ltd., Tokyo, Japan) at 298 K, adjusting pH of the slip with an aqueous solution of 3N-NaOH and 3N-HCl.

2.4 Forming

Metal cylinders that each had a volume of 3 cm^3 were placed on molds with cylindrical cavities as reservoirs. The three kinds of slips with minimum viscosity were poured into the cylindrical and dumbbell-type molds. The castings were separated from the molds after absorption of water for two days and were dried in an oven at 353 K for 3.6 ks.

2.5 Green density and strength

Green densities of the cylindrical castings were calculated by measuring the weights and sizes of the casting. Green strengths were examined by three point-bending of the cylindrical castings. The strength was measured with a material testing machine (IS-5000, Shimazu Co. Ltd., Kyoto, Japan) with the gauge length of 20 mm and the cross-head speed of 8.33×10^{-3} mm/s. Green density and strength both were measured five times.

2.6 Sintering

Each cylindrical casting was cut into three discs of 8 mm in length. The three discs were placed in titanium foil boxes with sponge titanium granules and heated in a high alumina

tube in an electric furnace with a heater of SiC at a heating rate of 4.72 K/s in an argon atmosphere after evacuation of air from the tube and were then kept at 1373, 1473 and 1573 K for 3.6, 7.2 and 10.8 ks, respectively. These sintered discs were used for measurement of linear shrinkage, relative density and hardness and for observation of microstructure. The sintered discs were cooled in the furnace to room temperature under the same atmosphere. Dumbbell-type castings for tensile tests were sintered under the same condition of the atmosphere at 1473 K for 7.2 ks.

2.7 Linear shrinkage and relative density

Linear shrinkage was calculated by measuring the lengths of the sintered disc before and after sintering. Relative density was calculated at the ratio of bulk density of the sintered disc to theoretical density of titanium (4.5 kg/m^3). Bulk density was measured on the basis of Archimedes' principle of buoyant force. For each W/P the measurements were done in triplicates, and the bulk density was considered the mean values.

2.8 Tensile strength, elongation and hardness

Tensile tests were performed three times for the sintered dumbbell-type castings produced from slips with different W/P ratios using the same material-testing machine operated with a crosshead speed of 8.33×10^{-3} mm/s. The gauge length of the sintered dumbbell-type castings was set to be 20 mm for calculation of elongation. Tensile strengths are mean values for three castings produced from three slips with different W/P ratios. Elongation was calculated on the basis of the gauge lengths before and after the tensile test. Tensile tests of commercial wrought Ti plates (JIS H4657, No.2) also were also performed as control materials along with the hardness measurement. In order to measure hardness, the above sintered discs were embedded in epoxy resin and then ground with SiC paper and polished with a suspension of aluminum particles. A micro-Vickers hardness-testing machine (M model, Shimazu Co. Ltd., Kyoto, Japan) with a load of 0.5 kg and loading time of 15 s was used. For each W/P ratio the hardness were measured in ten points.

2.9 Microstructure and fractured surface

All the sintered discs were examined by X-ray diffractometer (JDX-3500, JEOL, Akishima, Japan) using a copper target with accelerated voltage of 3×10^4 V, tube current of 0.3 A and a step scan of 4.18×10^{-2} rad/s. Each sintered disc was fixed with a utility wax in the center of a window (25 mm in length × 16 mm in width) of an aluminum plate holder. The microstructures of sintered discs treated at different sintering temperatures and for different periods were observed. The sintered discs were embedded in epoxy resin and then ground with SiC paper and polished with a suspension of alumina particles. Each polished disc was immersed for several seconds in an etching solution consisting of HCl (1 1.5 cm^3), HNO_3 (2.5 cm^3), HF (1.1 cm^3) and water(95 cm^3). The microstructures of the sintered discs after etching were observed with a light microscope (OPTIPHOT, Nikon, Tokyo, Japan), and photographs of the microstructures were taken using a digital camera (COOLPIX 950, Nikon, Tokyo, Japan). The tensile fractured surface of the dumbbell-type casting sintered at 1473 K for 7.2 ks was observed with a scanning electron microscope (S-4000, Hitachi, Tokyo, Japan). Mapping images of elemental distributions of the same sintered discs as those used for observation of the microstructure with the light microscope were examined with an electron-microprobe analyzer (JXA-8900M, JEOL, Akishima, Japan).

2.10 Statistical analysis

One-way analysis of variance was used to examine statistical differences in physical and mechanical properties of green and sintered castings using the program Multi-Tokei (SRI, Tokyo, Japan)

3. Results

Figure 4 and Fig. 5 show the relationships between the viscosities of slips and pH. Figure 4 presents the viscosities of

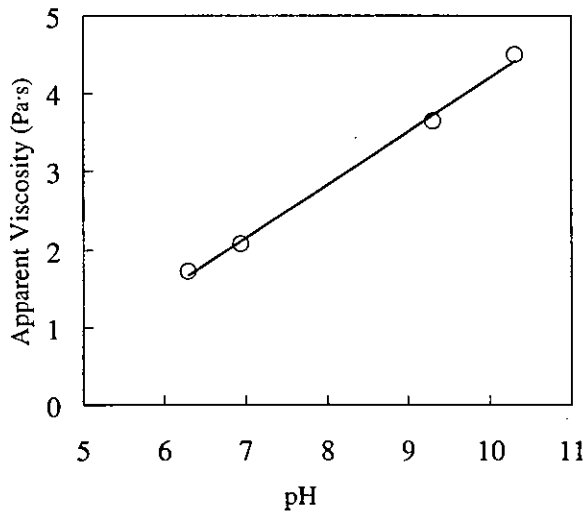

Fig. 4 Apparent viscosity of a slip vs. pH adjusted with NaOH solution in the case of a slip with a W/P ratio of 0.354.

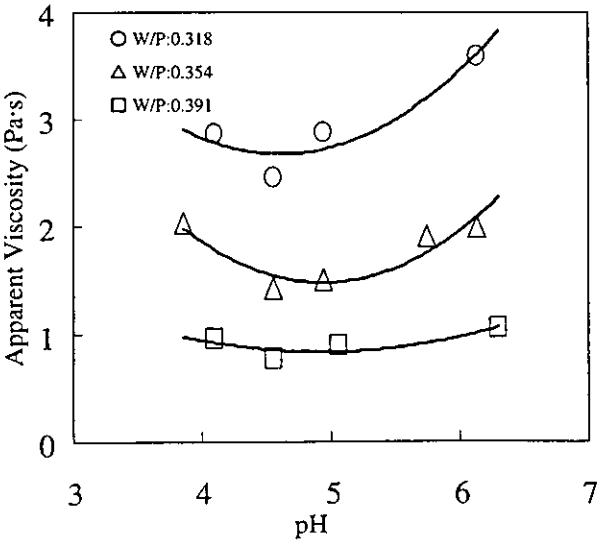

Fig. 5 Apparent viscosity of slips vs. pH adjusted with HCl solution for slips with W/P ratios of 0.318, 0.354, and 0.391.

a slip with a W/P ratio of 0.354 in the alkaline range adjusted with 3N-NaOH solution. The viscosity increased linearly from 1.720 Pa·s at pH of 6.30 to 4.4933 Pa·s at pH of 10.31 with addition of 3N-NaOH solution. On the other hand, addition of 3N-HCl solution lowered the pH of the three slips as shown in Fig. 5. The viscosities of slips with W/P ratios of 0.318, 0.354 and 0.391 decreased from 3.5933 Pa·s to a minimum of 2.4533 Pa·s, from 1.9950 Pa·s to a minimum of 1.4200 Pa·s, from 1.0583 Pa·s to a minimum of 0.7800 Pa·s, respectively. The viscosities of all three slips had a minimum at pH of about 4.5, decreasing with decrease in pH. Viscosity decreased considerably with a slight increase in W/P ratio.

Figure 6 shows the green densities and strengths of castings produced from slips with different W/P ratios. For the investigated W/P ratios there was no significant difference in the bulk densities of the castings. ($p > 0.05$). The green densities of all castings were about 2.20 kg/m^3. A significant difference was found between the green strengths ($p < 0.05$). Mean green strengths of castings produced from slips with W/P ratios of 0.318, 0.354 and 0.391 were 2.31, 3.09 and 3.82 MPa, respectively.

Figure 7 and Fig. 8 show the linear shrinkages and relative densities of the sintered castings produced from the three slips at different sintering temperatures for different periods. There was no significant difference between degrees of shrinkage or between densities of the sintered castings ($p > 0.05$). The degrees of linear shrinkage of sintered castings produced from slips with W/P ratios of 0.318, 0.353 and 0.391 varied from17.3 to 20.5, 16.6 to 20.5 and 17.6 to 20.1%, respectively. The relative densities of all sintered castings ranged from about 0.82 to 0.97.

Figure 9 shows the tensile strengths and degrees of hardness of sintered castings produced from the three slips under sintering conditions of 1473 K and 7.2 ks. The mean tensile strengths of sintered castings produced from slips with W/P ratios of 0.318, 0.353 and 0.391 were 259.5, 244.8 and 241.5 MPa, respectively. There was no significant difference between tensile strengths or degrees of hardness of the sintered castings ($p > 0.05$). The tensile strengths of the sintered castings ranged from 199.5 MPa when a slip with a W/P ratio of 0.354 was used to 302.3 MPa when a slip with a W/P ratio of 0.391 was used. The mean tensile strength of commercial wrought titanium plates was 389.0 MPa. The results of tensile tests showed that fractures of the sintered castings occurred in the straight portions of load-elongation curves. The elongations of the sintered castings were

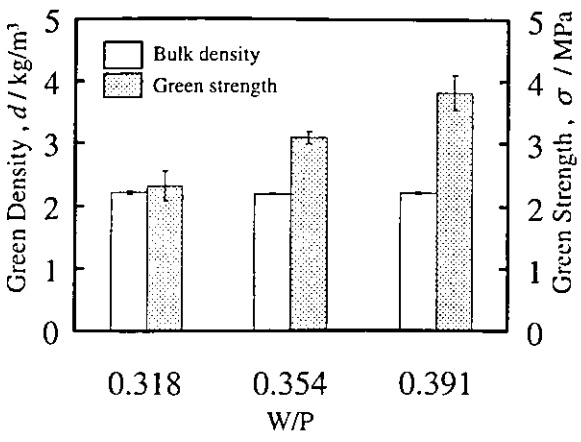

Fig. 6 Green densities and strengths of castings.

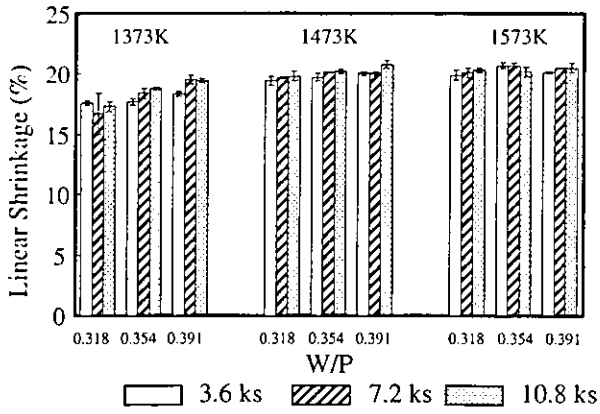

Fig. 7 Linear shrinkage of castings produced from slips with W/P ratios of 0.318, 0.354 and 0.391 and sintered at 1373, 1473 and 1573 K for 3.6, 7.2 and 10.8 ks.

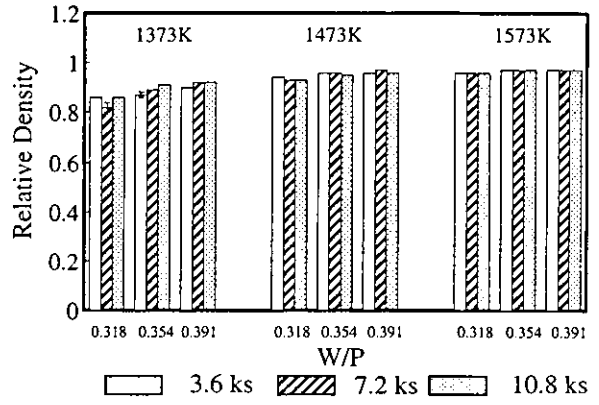

Fig. 8 Relative densities of castings produced from slips with W/P ratios of 0.318, 0.354 and 0.391 and sintered at 1373, 1473 and 1573 K for 3.6, 7.2 and 10.8 ks.

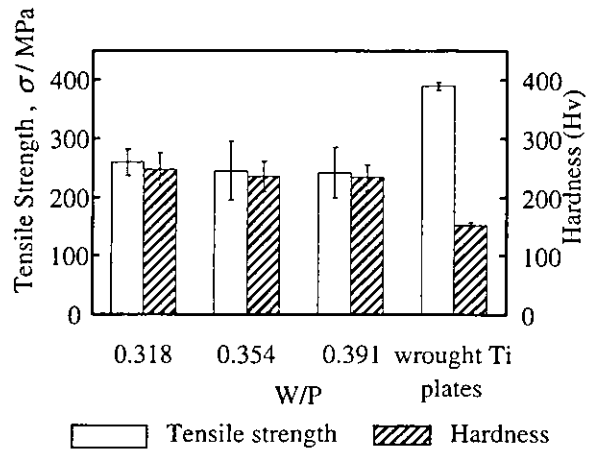

Fig. 9 Tensile strength and hardness of wrought Ti plates and castings produced from slips with W/P ratios of 0.318, 0.354 and 0.391 and sintered at 1473 K for 7.2 ks.

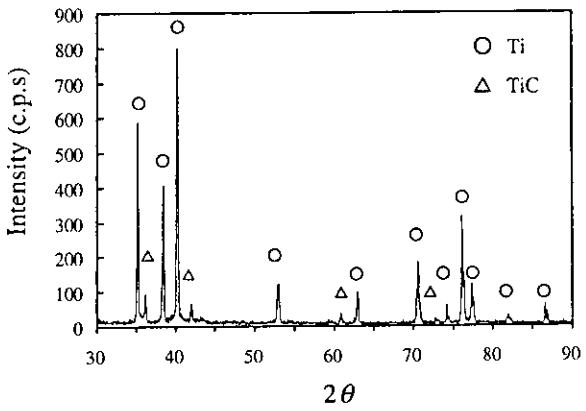

Fig. 10 X-ray diffraction pattern of a casting produced from a slip with a W/P ratio of 0.391 and sintered at 1373 K for 10.8 ks.

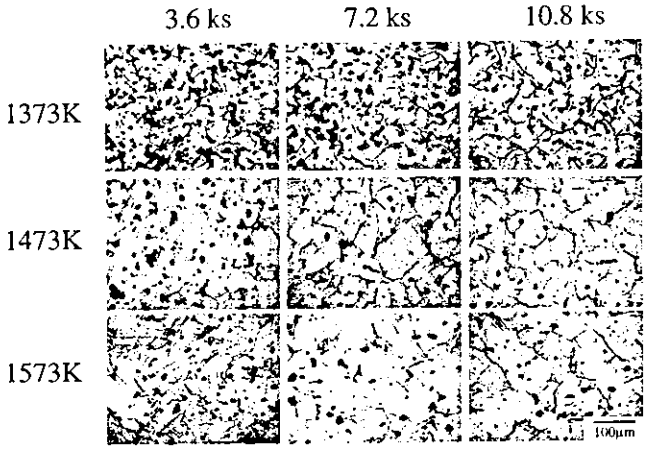

Fig. 11 Microstructures of the castings produced from slips with a W/P ratio of 0.318 and sintered at 1373, 1473, and 1573 K for 3.6, 7.2 and 10.8 ks.

negligible compared to that of wrought titanium plates of 45.3%.

Figure 10 shows an X-ray diffraction pattern of a casting produced from a slip with W/P ratios of 0.391 that had been sintered at 1373 K for 7.2 ks. Typical peaks of α-titanium and TiC were identified. Basic crystal structures of all other sintered castings were that of α-titanium, but specific peaks of TiC were not detected by X-ray diffractometry.

Figure 11 shows metallurgical structures of sintered castings produced from a slip with a W/P of 0.318 that had been heated at different sintering temperatures and for different periods. At a sintering temperature of 1373 K, number of pores decreased with increase in sintering times. Higher sintering rates obtained at 1473 K and 1573 K produced fewer pores and the crystal grain growth was observed. The same metallurgical structures were also seen in castings produced from slips with W/P ratios of 0.354 and 0.391 that had been sintered at the same temperatures and time. Rod-like precipitates were found in all of the sintered castings (See also Fig.12(a).).

Figure 12 shows SEM images and mapping images of elemental distribution in a casting produced from a slip with a

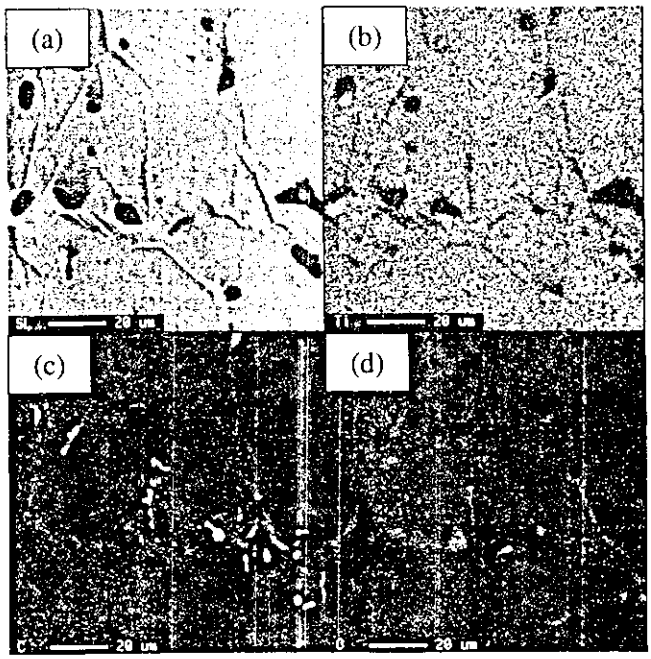

Fig. 12 Mapping images of elemental distribution of a casting produced from a slip with a W/P ratio of 0.391 and sintered at 1373 K for 10.8 ks. (a) SEM image, (b) Ti, (c) C, (d) O

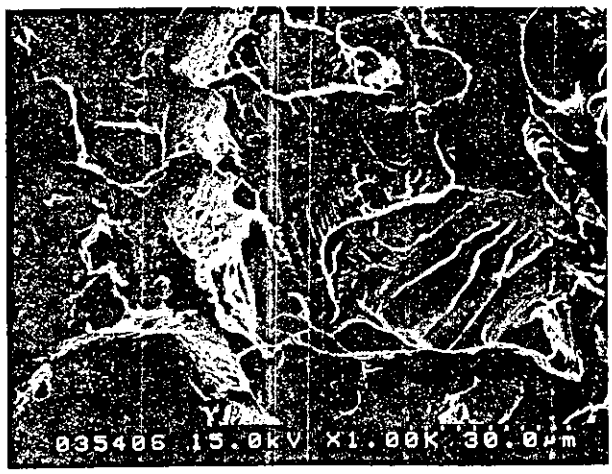

Fig. 13 SEM image of the tensile fractured surface of a casting produced from a slip with a W/P ratio of 0.354 and sintered at 1473 K for 7.2 ks.

W/P ratio of 0.391 that had been sintered at 1573 K for 7.2 ks. Carbon and oxygen were detected by EPMA through the sintered casting. Second phases were observed along the crystal grain boundaries of the sintered casting as long and narrow precipitates. The precipitates were composed of titanium, carbon and oxygen

Figure 13 is the fractured surface of a tensile casting produced from a slip with a W/P ratio of 0.354 that had been sintered at 1473 K for 7.2 ks. The fracture occurs through the crystal grains. Ridge patterns were observed on the fractured surface. Pores were also seen in crystal grains and along crystal grain boundaries. The same fractured surfaces were seen in sintered castings produced from slips with W/P ratios of 0.318 and 0.394.

4. Discussion

4.1 Influence of powder concentration on the slip viscosity

A Change in the W/P ratio of the titanium powder slip from 0.318 to 0.391 caused the viscosity of the slip to decrease considerably. In a thick suspension such as a slip, there is naturally interaction between titanium particles. These results suggest that adequate powder content is necessary for slips with desired fluidity. The viscosity of a dilute suspension with the volume fraction of particles less than 5% is given by Einstein's viscosity-formula.[20] According to the formula, the viscosity depends on viscosity of the medium and volume fraction of particles in the suspension. As the particle concentration in the slip is much higher then the 5% limit, the Einstein's formula fails to predict the slip viscosity. Norton *et al.*[21] developed a formula valid for the entire concentration interval, based on the flow properties of clay-water suspensions. The equation is based on the following independent effects: (1) viscosity of the liquid medium, (2) groups of particles and (3) interference of the particles.

4.2 Influence of sodium alginate and pH on the slip stability

A viscous medium such as alginate solution is used to produce a stable slip of metal powder by adjustment of pH[17,22] as discussed below. Particles in commercial metal powder in a suspension are usually small but sediment easily since the density of a metal powder is greater than that of a ceramic powder. The stability of a metal slip is affected more by density than by electric charges on the surfaces of particles. In the case of metal slips, the principle of the Stokes law is useful for obtaining a stable slip.[23] The law explains the rate of sedimentation of a particle in a liquid medium:

$$S = D^2(m_1 - m_2)g/18\mu \qquad (1)$$

where S is rate of sedimentation speed, D is diameter of a powder particle, m_1 and m_2 are densities of the powders and medium, μ is viscosity of the medium, and g is gravity constant. The rate of sedimentation is greatly influenced by the size of a particle and viscosity of the medium. The smaller the particles are and the more viscous the medium is, the more stable the slip is. Aqueous alginate solution as a medium also yields high viscosity even at a low concentration because of the macromolecular structure of alginate. Considering all the observations the slip of titanium is complex rheological system.

The Na alginate used in this study is a similar polyelectrolyte as PMMA-Na as mentioned below. Dissociation of the Na alginate and electric charges on titanium particles were not examined here in this study. It is thought that the alginate also partly dissociates into main chains with acid group $-COO^-$ and Na^+ in an aqueous solution. In the case of the titanium powder slip, by analogy with PMMA-Na, linearly dissociated groups of the alginate may be adsorbed on the titanium particles. The increasing viscosity of the slip with increase in pH indicates that the linear macromolecule chains shrink and become locked together on the addition of alkaline solution. The decrease in viscosity in the acid range is due to further dissociation of linear macromolecule chains of the alginate. The electric charges that are induced by the dissociation cause the releases of the intertwining of linear macromolecules because of their repulsive forces. In this stage of the study we cannot explain the observed increase of the slip viscosity for pH lower than 4.5. Further study is needed to determine the influence of the pH on the relationship between dissociation reaction of the Na alginate and surface electric charges of titanium particles.

The use of a polyelectrolyte such as Na polymethacrylate (PMMA-Na) to produce a stable casting slip for ceramic forming has also been proposed.[24] Dissociation of PMMA-Na increases with increase in pH of the solutions. Net surface charges on α-Al_2O_3 change from positive to negative with increasing pH. A-COO^- with dissociation of PMMA-Na is adsorbed on positively charged α-Al_2O_3 powder in a suspension. The negatively charged polyelectrolyte chains repel each other and the suspension becomes stable. The amount of PMMA-salt absorbed increases with decrease in pH in a stable suspension. Flocculation occurs in a stable suspension when pH has decreased to a level below the range for stability, because more PMAA is required to maintain the suspension stability at lower pH values.

Fluidity of a slip is a closely related to stability of the slip. Stability of a slip means that dispersed powders do not easily separate from a liquid medium by coagulation and sedimentation. Therefore, preparation of a stable slip is important for factors in the slip casting. The principle of colloid chemistry is applied for preparation of stable slips in the ceramic industry.[25] A colloidal particle has a fixed layer of ions absorbed on its surface with a diffuse layer of counter ions surrounding the fixed layer. These two layers are called an electric double layer. Zeta potential is generated between the interface of the double layer and the bulk of a solution.[26] As the zeta potential increases, mutual repulsion of these layers causes colloidal particles to become more stable without flocculation in the solution.

pH of the slip is often adjusted to lower the viscosity of the slip so that the slip can flow into easily a mold.[22,27,28] The viscosity of a ball-milled alumina slip decreases with reduction in pH by addition of HCl solution.[25] Hydrogen ions are adsorbed on the surfaces of alumina particles. Chloride ions acting as counter ions surround the layers of hydrogen ions on the surfaces of the alumina particles. The viscosity of the alumina slip is decreased by the effect of repulsive forces derived from such an electric double layer. However, excessive addition of acid solution causes the viscosity of the slip to increase reversibly.

4.3 Green density and strength

It is expected that both density and strength of a casting will increase with decreasing in the W/P ratio of the slip. The density and the strength are affected by the packing condition of powder particles in the casting. The powder concentration per unit volume of slip increases as the W/P ratio of the slip decreases. It is thought that higher density and strength can be obtained by reducing the W/P ratio. However the green density does not depend on the W/P ratio. Relative density of the castings, which is the ratio of green density to theoretical density of titanium (4.51 kg/m^3), was about 0.49. In other

words, the porosity is almost 50% for each W/P ratio. The castings have many pores that control the green density and the strength. The strength is actually influenced by the W/P ratio of the slip, but this is explained not by the unchanged density but by the difference in adhesive power of the alginate as a bonding material in each slip. The adhesive power increases with the W/P ratio of the slip. In pressure forming,[13,29] green densities have been reported to vary from 2.11–3.34 kg/m^3 or 3.40–4.17 kg/m^3, depending on particle sizes of titanium powder and compacting pressure, and the green compressive strengths have been reported to range from 0.62–102.62 MPa. The green densities and the green compressive strengths increased with increase in particle sizes of the powder in the pressing. The green densities obtained by slip casting are similar to those partly compared to ones obtained by pressure forming.

4.4 Linear shrinkage and relative density

During the sintering process the contact area between the particles increases while the porosity decreases.[30] The higher the sintering temperature is, the greater is the rate of sintering. Both sintering shrinkage and relative density are measures of densification in sintering of powder densification.[31,32] Densification is also affected by particles sizes of powder,[33] forming pressure,[34] the sintering atmosphere.[35] In pressure forming,[13] linear shrinkages and densities of titanium compacts sintered in a high vacuum for 3.6 ks at 1373 K varied from 3.97 to 21.9% and from 3.05 to 4.44 kg/m^3, respectively. Green densities of slip castings are less than those of with pressure-formed compacts because slip casting is a process of non-pressure forming. The casting structure is highly porous proved by the small value of the relative density of 0.49. The relative densities of all slip castings sintered for 3.6 ks at 1372 K were about 0.84. Increasing the sintering temperature and time the final relative density increased up to 0.97. The Densification produced by the sintered castings comparable to that of the pressure forming. It was reported that the rate of densification in sintering of a slip casting was considerably greater than that of a pressure-forming compact, because of the transport of materials during the forming, larger amounts of point lattice defects, different types of pores and faster grain boundary movement.[36]

4.5 Microstructure and phase analysis

Sintered materials have a polycrystalline structure that includes pores. Crystal grain growth is also observed during the sintering. When a slip with a W/P ratio of 0.318 was used, the casting sintered at 1373 K had many pores compared with castings sintered at temperatures of 1473 and 1573 K, indicating that a higher sintering temperature promotes sintering of casting. Similar changes in microstructure were observed when slips with W/P ratios of 0.354 and 0.391 were used.

Titanium has a hexagonal close packed structure (α-phase) at a room temperature and is transformed into body center cubic structure (β-phase) at 1155 K. Since the sintering temperature is well over α-β transition temperature the titanium in the sintered castings are β-phase. After cooling in the furnace, the X-ray diffractometry comfirmed that titanium is in a α-phase. It has also been reported that α-β cycling heating by programmed heating and cooling promotes the sintering.[37] Our sintering temperatures were over transition temperature, so all the effects reported occurred in our sintered castings.

4.6 EPMA analysis

The oxygen and carbon detected in the sintered castings by EPMA are derived mainly from the binder of sodium alginate. Sodium alginate is decomposed thermally into simple carbon, hydrogen gas, carbon monoxide and gaseous sodium in the sintering process. Since the titanium particles in green casting are covered with the alginate, it is thought that the decomposed carbon dissolve into lattice of titanium in the sintering process and during slow cooling precipitates as TiC along the crystal grain boundary as shown in Fig. 12. The existence of TiC was also confirmed by XRD as shown in Fig. 10. Furthermore, the results of EPMA suggest that the precipitated TiC phase contains oxygen and is expressed as Ti(C, O). Usually, organic binders are also necessary in an injection mold of metal powder. TiC occurs for reaction of titanium powder with an organic binder in a sintering process.[38,39] Formation of TiC depends on the conditions of debinding before the sintering, the type of the binders and addition of TiH powder.

4.7 Tensile strength and hardness

The tensile strengths of the sintered castings were less than those of the wrought titanium plates. Load-elongation curves obtained from the tensile tests indicate that the sintered castings are brittle without plastic deformation. The bulk densities of the sintered castings produced from the three slips with different W/P ratios are all about 0.96, near the theoretical value. The degree of porosity does not seem to be related to the tensile strength of the sintered castings. It is thought that strength of the base titanium affects the strength of the sintered castings.[40,41] The results of EPMA and XRD show that oxygen and carbon harden the base titanium and that TiC exists along crystal grain boundaries. A crack occurs near a pore because of stress concentration and propagates easily through the hard base titanium and along the crystal grain boundaries with TiC. As shown in Fig. 13, fractography after the tensile tests indicated that fractures were generated through decohesion at the interface between the precipitate and matrix. As a result, the surface showed a ridge pattern that is typical of brittle fracture. In plasma-activated sintering,[14] the tensile strength of sintered titanium with a density of 4.5 was 650–760 MPa. Recently the metal injection molding process,[42] the tensile strength was shown to be 550–720 MPa in sintered titanium with a relative density of 0.97–0.99. The tensile strengths of the sintered titanium produced from the above two different methods were greater than those of wrought titanium plates. However, the hardness of the sintered castings was greater than that of wrought titanium plate. The dissolved oxygen and carbon affect the hardness of the sintered titanium.

The microstructures of the sintered castings need to be modified so that they do not contain amounts of oxygen and carbon exceeding the specified amounts of the Japanese Industrial Standards[43] in order to improve their mechanical properties. Possible methods of modification are proposed as

follows.: (1) use of high-vacuum sintering, (2) nonuse of the alginate, and (3) only use of water as a medium by applying powder of colloidal particle sizes.

REFERENCES

1) D. F. Williams: *Biocompatibility of Clinical Implant Materials*, (CRC Press, Inc Boca Raton, Florida, 1984) pp. 7–44.
2) P.-I. Bränemark: J. Prosthet. Dent. **50** (1983) 399–410.
3) E. D. Rekow: J. Prosthet. Dent. **58** (1987) 512–516.
4) F. Duret *et al.*: J. Am. Dent. Assoc. **117** (1988) 715–720.
5) T. Sohmura, J. Takahashi: J. Jpn. Dent. Mater. **13** (1994) 61–66 (in Japanese).
6) R. M. Waterstrat: Publication No. (NIH) 77-1227, (US. Dept.Health, Education and Welfare, Washington DC) (1977) 224–233.
7) T. Togaya, M. Suzuki, K. Ida, M. Nakamura, T. Uemura and S. Okuda: J. Jpn. Dent. Mater. **4** (1985) 344–349 (in Japanese).
8) K. Ida, T. Togaya and M. Suzuki: J. Jpn. Dent. Mater. **2** (1983) 765–771 (in Japanese).
9) E. H. Greener, J. B. Moser, J. Opp, K. Szurgot and B. C. Marker: J. Dent. Res. **65** (1986) 317 (abstract 1329).
10) H. Hashimoto, A. Kuroiwa, K. Wada, Y. Kouchi, T. Hashimoto, Y. Hasegawa, Y. Ando and Y. Akaiwa: J. Jpn. Dent. Mater. **11** (1992) 603–614 (in Japanese).
11) I. Miura and K. Ida *et al.*: *Chitan no Shika Riyou* (Quintencence Book, Tokyo, Japan, 1988) pp. 161–266. (in Japanese).
12) T. Okabe and H. Herø: Cell and Mat. **5** (1995) 211–230.
13) Y. Oda: J. Jpn. Dent. Mater. **3** (1984) 376–400.
14) W. S. Lee :J. Jpn. Dent. Mater. **14** (1995) 142–154.
15) R. A. Fuy, JR, R. G. Craig and K. Asgar: J. Oral. Rehabil. **3** (1976) 151–160.
16) W. D. Kingery *et al.*: *Ceramic fabrication processes*, (The M.I.T. Press, Cambridge, Massachusetts, 1968) pp. 5–51.
17) P. E. Rempes, B. C. Weber and M. A. Schwartz: Cera. Bull. **37** (1958) 334–339.
18) W. E. Hauth: J. Am. Cera. Soc. **32** (1949) 394–398.
19) ASM: *ASM Handbook*, Vol. 7, 1st ed., (ASM International, Ohio, 1998) 162–163.
20) T. Nakagawa and H. Kanbe: *Rheology*, 8th ed., (Misuzu Shobo Co., Tokyo, 1969) pp. 624–627.
21) F. H. Norton, A. L. Johnson and W. G. Lawrence: J. Am. Ceram. Soc. **27** (1944) 149–164.
22) H. V. Sulinski: U. S, Govern Res. Re. AD 432235, (1964) 26PP.
23) H. H. Hausner and D. P. Ferriss: Materials & Methods, **43** (1956) 132–134.
24) J. Cesarano and I. A. Aksay: J. Am. Ceram. Soc. **71** (1988) 250–255.
25) W. E. Hauth: J. Phys. Colloid Chem, **54** (1950) 142–156.
26) S. Glasstone and D. Lewis: *Elements of Physical Chemistry*, 2nd ed., (D. V. Nostrand Co. Maruzen Co., Tokyo, 1968) pp. 579–580.
27) P. D. S. St. Pierre: Trans. Brit. Ceram. Soc, **51** (1952), 260–268.
28) P. D. S. St. Pierre: Proc. 3rd annual conf.; Reactive Metal,ed. by W. R. Clough, (Interscience, Buffalo, New York,1958) pp. 93–107.
29) M. J. Jr. Donachie: *Titanium a technical guide*, 2nd ed., (ASM, International, Materials Park, Ohio, 2000) pp. 96–97.
30) ASM: *Metals Handbook*, Vol. 9, 9ed., (ASM, Metals Park, Ohio, 1984) pp. 308–321.
31) W. D. Kingery etal: *Ceramic fabrication processes*, 4th ed., (The M.I.T. Press, Cambridge, Massachusetts, 1968) pp. 120–131.
32) W. Raja and R. F. Boehm: J. Den. Res. **53** (1974) 1351–1354.
33) ASM: *Metals Handbook*, Vol. 7, 9ed (ASM, Metals Park, Ohio, 198) pp. 309–310.
34) W. D. Kingery: *Kinetics of high-temperature processes*, The M.I.T. Press, Cambridge, Massachusetts, John Wiley Sons, New York, Chapman & Hall, London, 1959) pp. 158–159.
35) ASM: *Metals Handbook*, Vol. 4, 8ed. (ASM, Metals Park, Ohio, 1986) pp. 455–457.
36) H. H. Hausner: J. Jpn. Soc. Powder and Powder Metall. **7** (1960) 58–72.
37) Akechi, K., and Hara, Z.:Proc. 2nd Int. Conf. on Titanium'**80**, Science and Technology, vol. 3. (Metall Soc.AIME, 1973) 2255–2263.
38) H. Kyogoku, T. Toda and K. Shinohara: J. Jpn. Soc. Powder and Powder Metall. **40** (1993) 440–443.
39) H. Kyogoku, S. Komatsu, I. Tsuchitori and T. Toda: J. Jpn. Soc. Powder and Powder Metall. **42** (1995) 1052–1056.
40) T. Kono, A. Horata and T. Kondo: J. Jpn. So. Powder and Powder Metall. **44** (1997) 985–992.
41) K. Majima, T. Isono and K. Shoji: J. Jpn. Soc. Powder and Powder Metall. **33** (1986) 28–33.
42) K. Kusaka, T. Kohno, T. Kondo and A. Horata: J. Jpn. Soc. Powder and Powder Metall. **42** (1995) 383–387
43) JSA: JIS H 4650, (JSA, 2001) pp. 1–16.

Three-Dimensional Topographic Scanning Electron Microscope and Raman Spectroscopic Analyses of the Irradiation Effect on Teeth by Nd:YAG, Er:YAG, and CO_2 Lasers

Magda K. Yamada, Motohiro Uo, Shoji Ohkawa, Tsukasa Akasaka, Fumio Watari

Dental Materials and Engineering section, Department of Oral Health Science, Graduate School of Dental Medicine, Hokkaido University, Kita 13, Nishi 7, Kita-ku, Sapporo 060-8586, Japan

Received 27 August 2003; revised 9 January 2004; accepted 10 January 2004
Published online 4 May 2004 in Wiley InterScience (www.interscience.wiley.com). DOI: 10.1002/jbm.b.30063

Abstract: A three-dimensional analyzer installed in a scanning electron microscope was used to evaluate the morphology and surface roughness using noncontact profilometry. Observations were carried out on the enamel and dentin surface irradiated by three different lasers: Nd:YAG (wavelength 1.06 μm), Er:YAG (2.94 μm), and CO_2 (10.6 μm). Spectroscopic analysis was done by Raman spectroscopy for nonirradiated and laser-irradiated surfaces. The lasers were applied perpendicularly to vertically sectioned and polished human extracted caries-free molars. The tooth was sectioned at each cavity for cross-section analysis after laser irradiation. Irradiation by Nd:YAG and CO_2 lasers of the enamel surface showed an opaque white color, different from dentin where the surface turned black. The Er:YAG laser induced no changes in color of the dentin. Numerous cracks associated with thermal stress were observed in the CO_2 laser-irradiated dentin. Noncontact surface profile analysis of Er:YAG laser-irradiated enamel and dentin showed the deepest cavities, and direct cross-sectional observations of them showed similar cavity outlines. The CO_2 laser-irradiated dentin had the least surface roughness. Raman spectroscopic analysis showed that fluorescence from the laser-irradiated tooth was generally greater than from nonirradiated teeth. Bands in dentin attributed to organic collagen matrix were lost after Nd:YAG and CO_2 laser irradiation, and a broad peak due to amorphous carbon appeared. The Er:YAG laser-irradiated dentin showed no sign of a carbon band and had more suitable results for dental ablation. Noncontact surface profile analysis was effective to evaluate the structural change in the tooth in the microarea of study after laser irradiation. © 2004 Wiley Periodicals, Inc. J Biomed Mater Res Part B: Appl Biomater 71B: 7–15, 2004

Keywords: laser; scanning electron microscope; Raman spectroscopy; tooth; surface roughness

INTRODUCTION

The ruby laser was developed by Maiman in 1960.[1] Goldman et al.[2] described the ruby laser application in relation to dental hard tissues in 1964, and suggested the possibility of its use to remove dental caries. The possibility of replacing the conventional treatment of using a bur with laser treatment has been investigated. Although ablation of dental hard tissue is possible by using a ruby laser, a higher energy density is needed, causing damage to the dental pulp. Studies have used other lasers in dentistry, such as Nd:YAG (wavelength 1.06 μm), Er:YAG (2.94 μm), and CO_2 (10.6 μm).[3–6]

Various imaging observations have been used to analyze and compare the effect of lasers on teeth. Watari[7] observed the effect of CO_2 laser irradiation using a scanning electron miscroscope (SEM), confocal laser scanning microscope (CLSM), and atomic force microscope to examine the same area of human teeth, and observed partial melting on the teeth surface. SEM observation has shown cracks and melting after Nd:YAG laser irradiation.[8] After Er:YAG laser irradiation, the opening of dentinal tubules and the tooth surface with microirregularities without a smeared layer have been observed that suggested the use of a laser as a substitute for acid etching before applying composite resin.[9] However, surface roughness (Ra) analysis is also needed, and is fundamental for correct evaluation. A conventional stylus profilometer has been usually used to measure roughness, but the measurements are separate from SEM imaging. The surface roughness value measured by a different device might not provide a comprehensive picture of the surface.[10] Also, the conventional stylus profilometer often damages dental hard tissue because of its direct contact with the specimen. Therefore, it

Correspondence to: M. K. Yamada (e-mail: magda@den.hokudai.ac.jp)

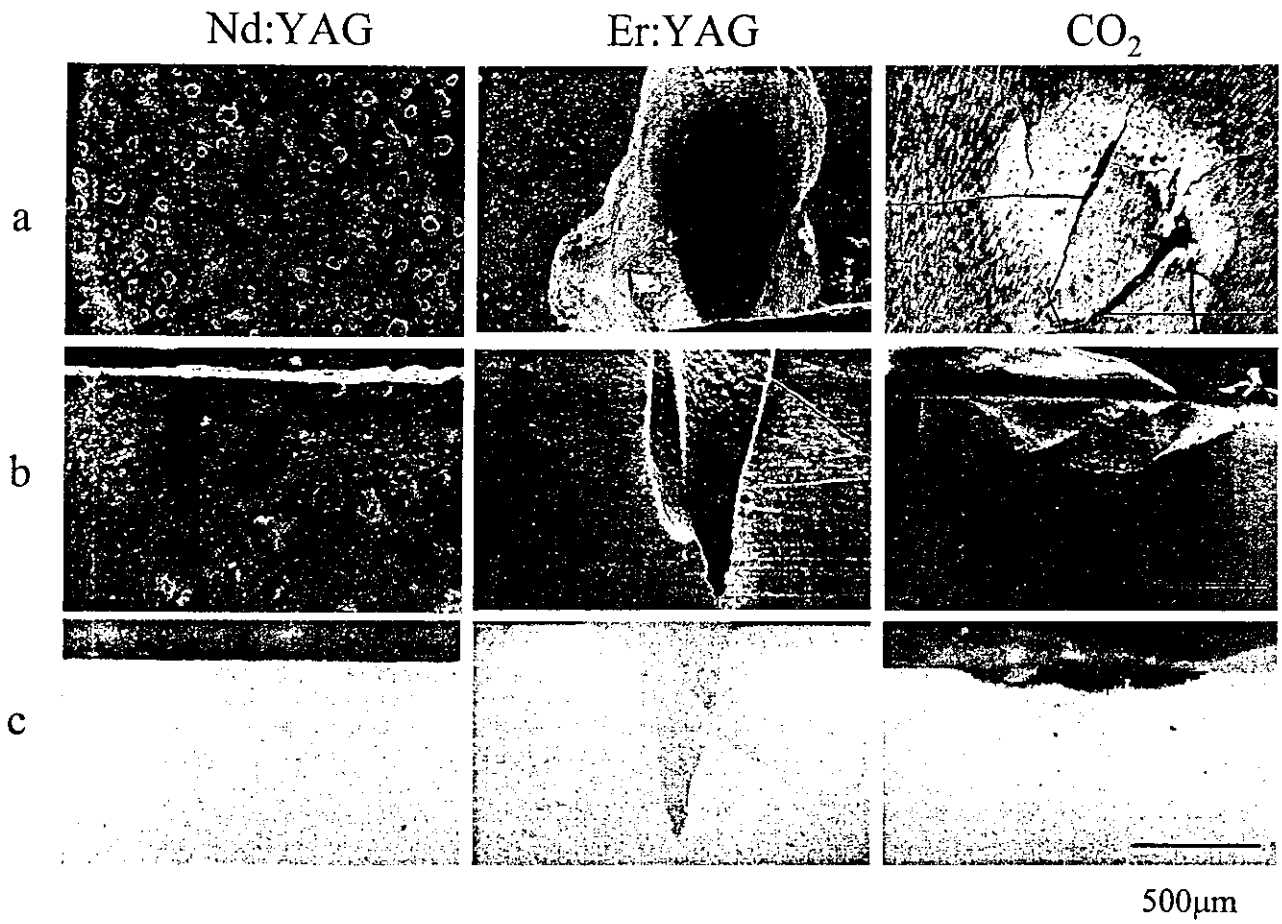

Figure 1. Dentin irradiated by Nd:YAG, Er:YAG, and CO_2 lasers. (a) SEM observation of top view, (b) vertical cross-section, and (c) digital microscopic view of cross-section.

describes surface characteristics by using a method that can give information on both surface morphology and roughness is important. SEM has a higher resolution, and can make observations without the teeth being coated if a low accelerating voltage is used. However, it usually only provides observational results. Recently, an SEM installed with a three-dimensional analyzer (3D-SEM) has been developed that uses reflection electrons with a four-quadrant divided detector to provide quantitative surface analysis. The 3D-SEM allows quantitative analysis and imaging simultaneously in a noncontact mode without the risk of sample damage and with a high spatial resolution, allowing measurement of the surface on visually selected specimen microareas, and is, therefore, a promising tool.

Chemical characteristics after laser irradiation are also important. Raman analysis gives information about the chemical state without damage. Another advantage is the spatial resolution of about 1 μm allows the chemical and structural information to be obtained within a μm range.

This study aimed to combine simultaneously imaging and quantitative analysis of the surface morphology of teeth by using 3D-SEM and compositional information by using Raman spectroscopy to evaluate the effects of Nd:YAG, Er:YAG, and CO_2 lasers on enamel and dentin.

MATERIALS AND METHODS

Specimen Preparation

Freshly extracted, intact, caries-free human third molars were cleaned and stored in deionized water at 4°C until use. Vertical sectioning was done by using a low-speed diamond saw (Minitom, Struers, Copenhagen, Denmark) under running water. Slabs were cut 2 mm thick. The exposed enamel and dentin of the cut surfaces were then polished with alumina powder (2, 1, and 0.05 μm successively), and were rinsed and sonicated in deionized water to remove the polished debris. The specimens were kept wet in deionized water until laser irradiation.

Laser Irradiation

The laser apparatus were Nd:YAG laser (Tanaka Laser TLL 7000 PLUS, ATD Japan, Tokyo, Japan), Er:YAG laser (Erwin, Hoya Corp., Tokyo, Japan and J. Morita Corp., Kyoto, Japan), and CO_2 laser (Model Panalas C10, Panasonic, Osaka, Japan). Laser irradiation was used vertically to the enamel and dentin surfaces.

The Nd:YAG laser irradiation was applied at a single pulse of 0.6 J total energy (wavelength 1.06 μm) at a pulse

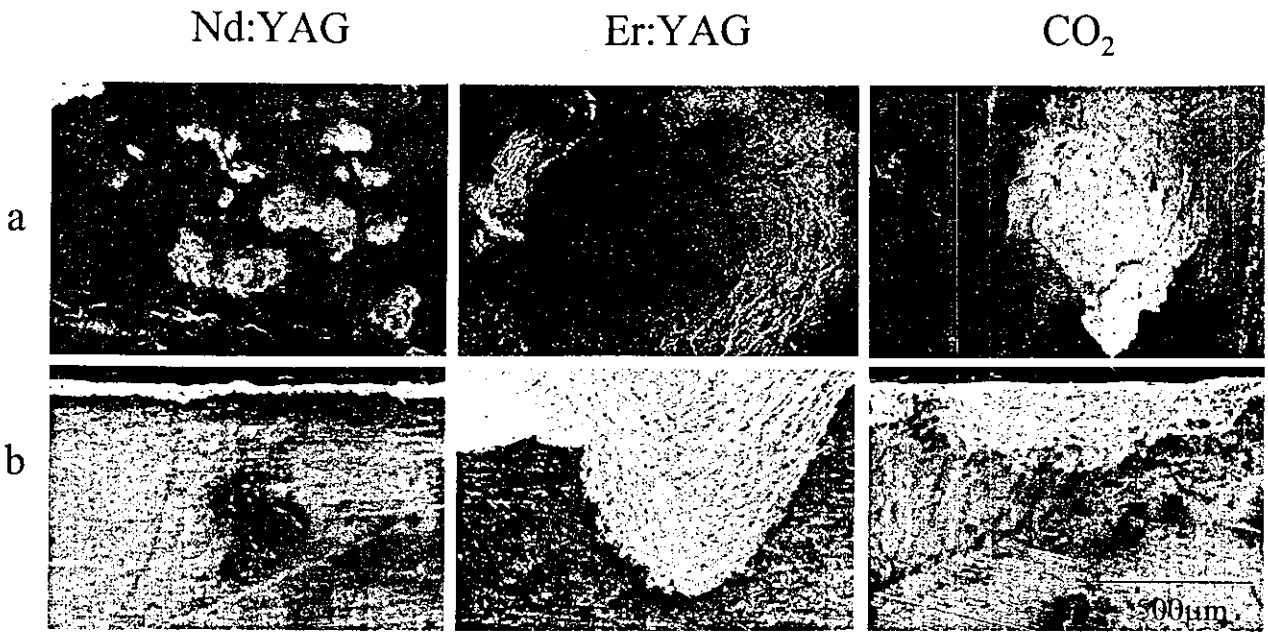

Figure 2. SEM observation of enamel irradiated by Nd:YAG, Er:YAG, and CO_2 lasers. (a) top view, (b) cross-section.

length 2 ms through a 2-mm diameter spot in noncontact mode. The work distance was fixed at higher than 1 mm. Carbon ink (Kaimei Carbon Ink, Kaimei Co. Ltd, Urawa, Japan) was applied to the surfaces before Nd:YAG laser treatment to absorb the laser beam efficiently.

The Er:YAG laser (2.94 μm) was applied at a total energy of 40 J for 20 s with a pulse repetition rate of 10 pulses per second (pps) and a probe diameter 4 mm under water spray with a work distance of approximately 1 mm.

The CO_2 laser (10.6 μm) was applied at a total energy of 4 J for the enamel and 3 J for the dentin surface. The pulse duration time was of 0.5 s, the diameter tip was 2 mm, and the work distance was approximately 1 mm. The laser was irradiated by using a single pulse.

For Er:YAG laser, the conditions were chosen according to the instructions of the manufacturer. For Nd:YAG and CO_2, the lasers were applied from low to high power to the tooth surfaces, and the power was selected in this order when modification of the tooth structure was observed by the naked eye.

Observation and Surface Analysis

Scanning Electron Microscope (SEM). The specimens were observed by using an SEM (Hitachi S-2380N and S-4700, Tokyo, Japan). Depth profile and 3D analysis was done by using a 3D analyzer (RD-500W) installed in the SEM (S-4700) by noncontact mode. The S-4700 operates by using a cold field emission electron source and has a high resolution at a low accelerating voltage. The device provides secondary electron (SE) and backscattered electron (BSE) images. The specimens were observed by using conventional SE at an accelerating voltage of 10 kV and by reflection electrons (RE) at 3 kV for SEM S-2380N and SEM S-4700, respectively. The same specimens were analyzed by using a Raman spectroscope without coating them with metal. After laser irradiation, the cavity was cut vertically and the cross-section was observed by using an SEM and a Digital Microscope (VH-6300, Keyence Corp., Osaka, Japan).

Raman Spectroscopy. Raman spectra of nonirradiated and laser-irradiated surfaces were obtained by using a Raman spectrometer (Labram, Horiba, Tokyo, Japan). Specimens were excited by He-Ne laser (632.8 nm) of 40 mW through a microscope objective lens (100×, NA = 0.90). The focal spot size was about 1-μm diameter. The spectra were recorded at resolution 2 cm^{-1}.

RESULTS

Figure 1(a) shows the top view of a dentin surface by SEM after Nd:YAG, Er:YAG, and CO_2 laser irradiation. The Nd:YAG laser-irradiated surfaces showed a layer of melted globules, the Er:YAG laser-irradiated surfaces showed an imbricate pattern, and the CO_2 laser-irradiated surfaces were smooth with numerous cracks associated with thermal stress. Observation of SEM [Fig. 1(b)] and digital microscope [Fig. 1(c)] show cross-sections after the laser-induced cavities were sectioned. Signs of carbonization in the dentin (black) were noted in the cross-sections after Nd:YAG and CO_2 laser irradiation in the views by digital microscope [Fig. 1(c)]. The cavity formed in the dentin by Nd:YAG laser irradiation was the shallowest at a depth of 0.03 mm, while Er:YAG produced a 1 mm deep, V-shaped cavity [Fig. 1(b, c)]. Although

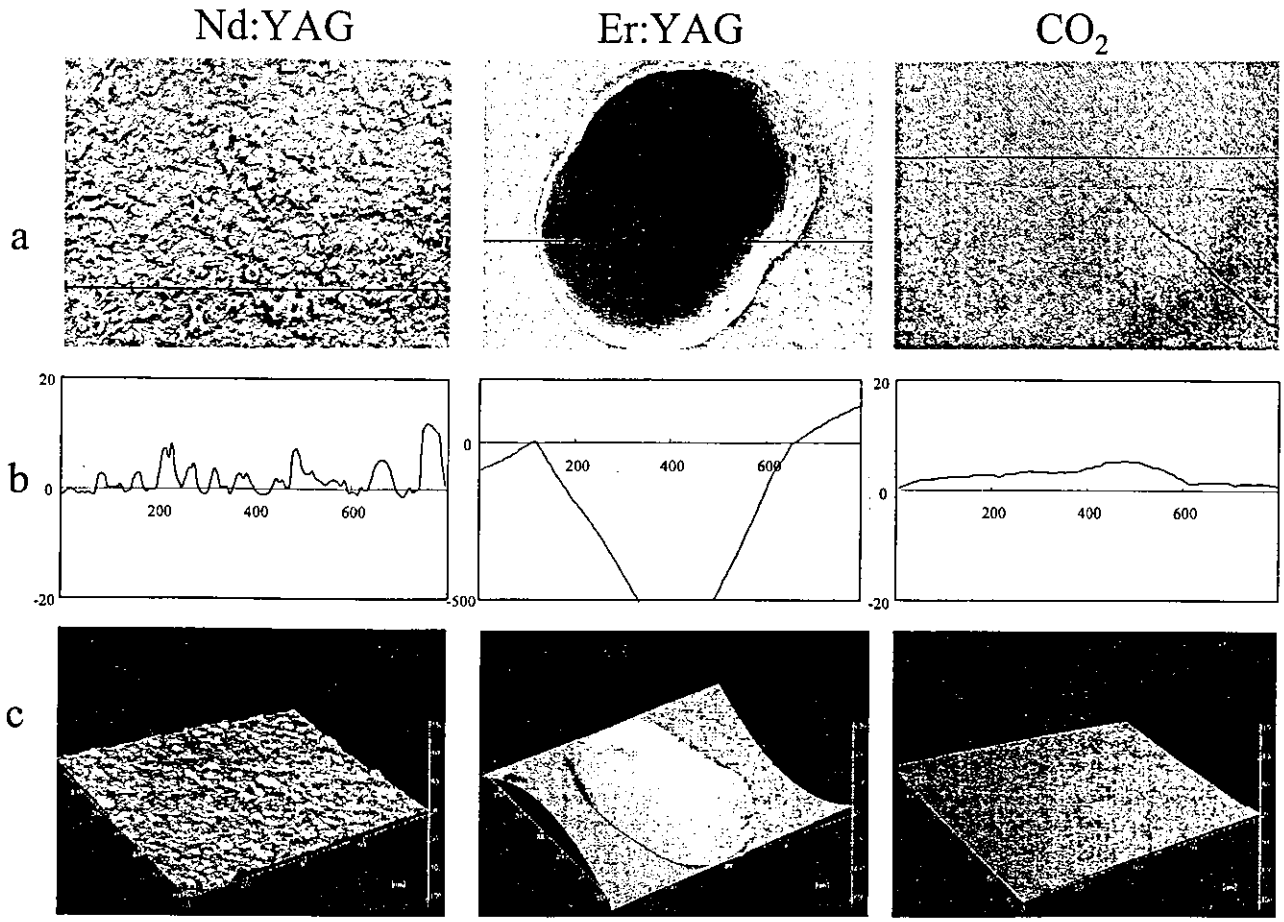

Figure 3. 3D-SEM analysis of Nd:YAG, Er:YAG, and CO_2 laser-irradiated dentin.(a) SEM images, (b) depth profiles, and (c) 3D images. Note that the depth scale in (b) of Er:YAG is larger by more than one order.

the CO_2 laser showed little ablation of the dentin surface in the macroscopic top view [Fig. 1(a)], the laser formed an arched cavity (black carbonized dentin) at a depth of approximately 0.1 mm in the cross-section [Fig. 1(b, c)]. Parts of the carbonized dentin were detached during the cross sectioning.

Figure 2 shows SEM images of the top view (a) and cross-sections (b) of enamel after Nd:YAG, Er:YAG, and CO_2 laser. Nd:YAG laser induced a flake-like morphology, the Er:YAG laser formed a deep cavity in which the surface has an imbricate pattern, and the CO_2 laser formed a crater-like surface. The depth of the cavities were 0.03 mm for Nd:YAG, 0.6 mm for Er:YAG and 0.1 mm for the CO_2 laser.

Figure 3 shows the top view (a), depth profiles (b) and 3D images (c) of laser-irradiated dentin surface by 3D-SEM. The depth profiles were obtained by noncontact mode along the horizontal line in the SEM image [Fig. 3(a)]. The depth scale of Er:YAG laser was larger by nearly 30 times. The approximately 7 μm high globules formed after Nd:YAG laser irradiation resulted in an Ra 2.23 μm. The smooth surface of the CO_2 laser-irradiated dentin gave an Ra of 1.09 μm. The deep and steep wall cavity formed by Er:YAG laser did not allow correct Ra analysis from the top view. However, the shape and depth of the V-shaped cavity was well reconstructed by the 3D image and showed topographically the dimension and spatial configuration of the surface modification. Comparison of the depth profiles obtained by noncontact mode [Fig. 3(b)] with the direct cross-sectional observation [Fig. 1(b, c)] showed approximately similar cavity outlines for Er:YAG laser irradiation. Details of the contours of the melted globules formed by Nd:YAG laser irradiation was difficult to observe in the direct cross-section at this magnification.

Figure 4 shows the same SEM analysis on the enamel surface. The cavity formed by Er:YAG laser was the deepest with a depth scale ten times larger. The scale in the vertical axis of the depth profiles of both dentin and enamel obtained by SEM is enhanced by Nd:YAG and the CO_2 laser and contracted by Er:YAG laser [Figs. 3(b) and 4(b)]. Due to the craters formed on the CO_2 laser-irradiated surface, Ra was 5.12 μm, rougher than Ra 3.42 μm of the Nd:YAG laser. Comparison of the depth profiles by using noncontact analysis [Fig. 4(b)] with the direct cross-sectional observation [Fig. 2(b)] showed approximately similar cavity outlines for Nd:YAG, Er:YAG, and CO_2 lasers.

As the deep and steep cavity of Er:YAG laser irradiation made difficult correct measurement of Ra from the top view,

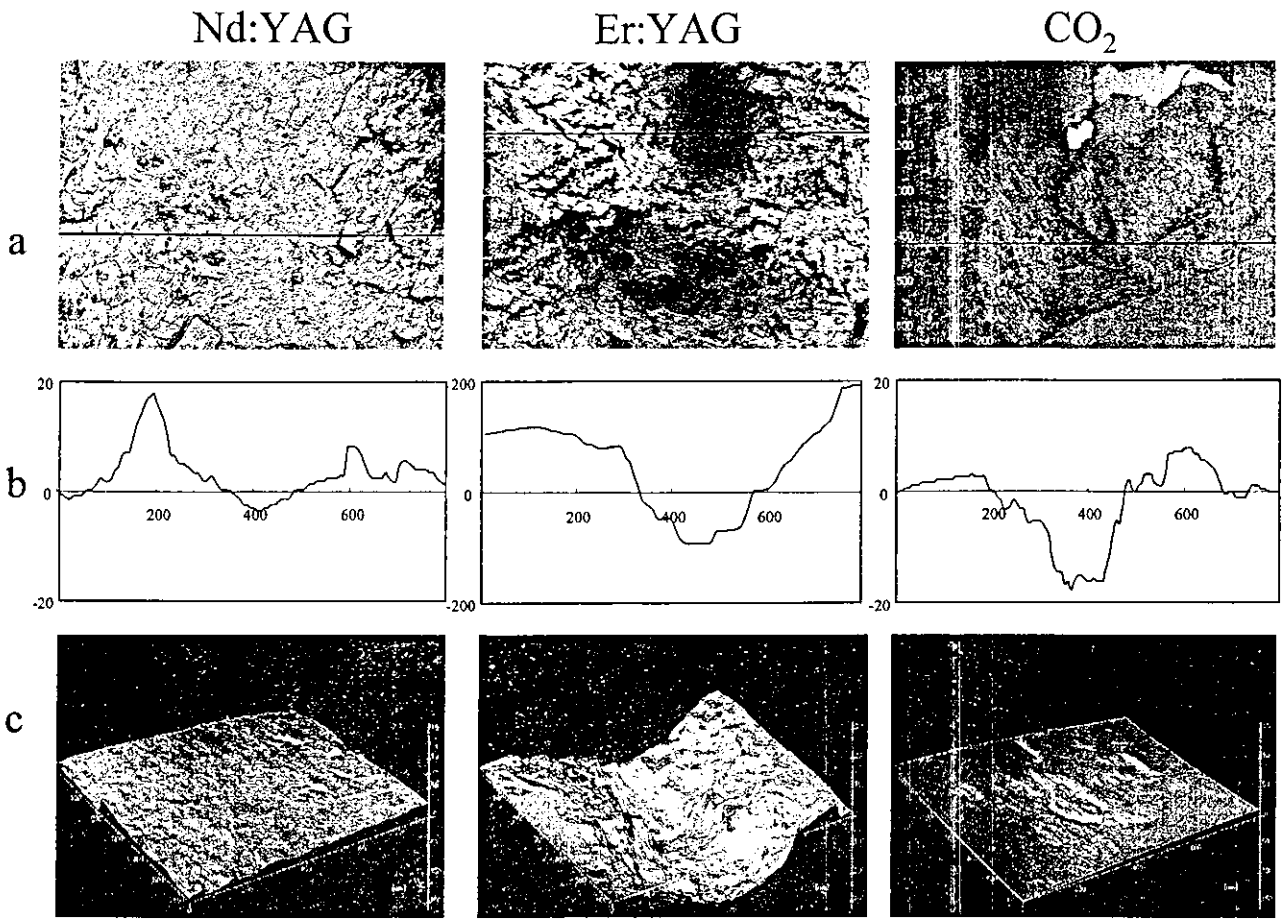

Figure 4. SEM observation of Nd:YAG, Er:YAG, and CO_2 laser-irradiated enamel. (a) SEM images, (b) depth profiles, and (c) 3D images. Note that the depth scale in (b) of Er:YAG is 10 times larger.

observation and analysis of both dentin and enamel were done after the cavity was cross-sectioned and the internal wall was laid horizontally (Fig. 5). The Er:YAG laser-irradiated dentin surface showed a smooth surface (Ra 2.5 μm) with open dentin tubules and a greater presence of peritubular dentin. The imbricate pattern observed on the enamel surface was Ra 12.22 μm, rougher than Nd:YAG and CO_2 laser irradiation.

Figure 6 shows the Raman spectra of nonirradiated (a) and laser-irradiated dentin (b). The background of the laser-irradiated surface was generally high compared with the nonirradiated surface. The Raman bands at ν_2 (350–500 cm^{-1}), ν_4 (550–650 cm^{-1}), ν_1 (900–1000 cm^{-1}) and ν_3 (1000–1130 cm^{-1}) represent the phosphate vibrations in hydroxyapatite. Bands attributed to the organic collagen matrix were at 1257, 1470, 1661, and 2945 cm^{-1} [Fig. 6(a), arrows]. These peaks were lost after Nd:YAG and CO_2 laser irradiation and broad peaks due to amorphous carbon were observed in the range of 1346–1580 cm^{-1} [Fig. 6(b)]. The Er:YAG laser-irradiated dentin surface showed no amorphous carbon band, which indicates few remnants on the surface.

Figure 7 shows the Raman analysis of the enamel surface. The background of laser-irradiated enamel was also higher than for nonirradiated enamel. The ν_2, ν_4, and ν_3 bands were not observed after Nd:YAG laser irradiation, while they were more visible by the Er:YAG and CO_2 laser irradiations.

DISCUSSION

Quantitative Analysis of Surface Roughness by SEM

The level of surface roughness needed for good bonding of a tooth with a composite resin is in the μm range. The often-used method to measure the Ra is the conventional stylus profilometer that is useful to analyze large areas, but it cannot be used to analyze selected microareas. The surface roughness of enamel prism, intertubular dentin, and peritubular dentin influences the bonding strength of a composite resin. These structures are in the microarea and selection of these areas by using a conventional stylus profilometer is not possible.

The CLSM can make noncontact analysis in selected microareas, but its resolution is lower than the 3D-SEM. The CLSM is advantageous because it uses subsurface analysis.

The 3D-SEM obtains the surface profile in a noncontact mode by reflection electrons, as well as a simultaneously image with high spatial resolution, allowing measurement of

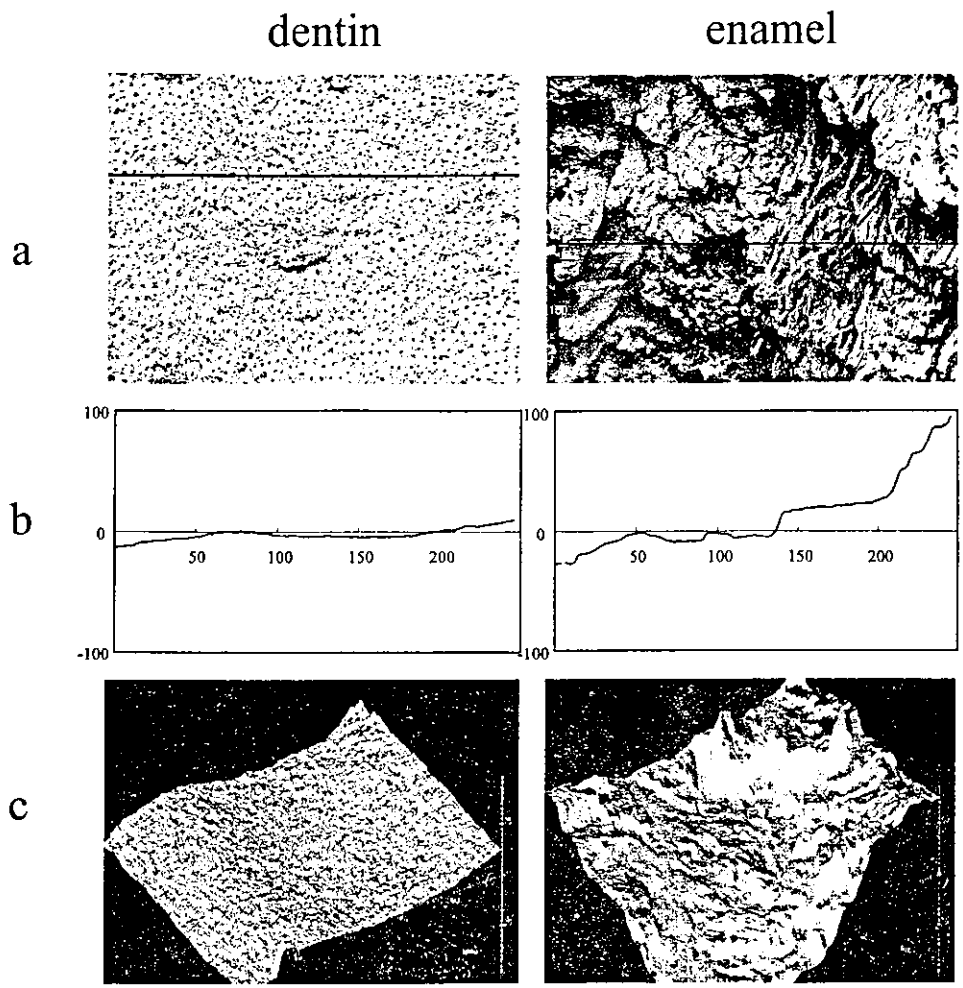

Figure 5. SEM observation of cavity wall made by Er:YAG laser irradiation on dentin and enamel. (a) SEM images, (b) depth profiles, and (c) 3D images.

a surface on visually selected specimen microareas, and gives a more exact surface profile of the images. The profile obtained by a noncontact mode also gives more details of the surface roughness.

Because the effect of a laser results in different morphological changes in microareas, selected microareas and high resolution for morphological analysis are needed. Therefore, results obtained from a 3D-SEM contribute to clarifying the understanding of a surface profile of laser-irradiated surfaces.

The 3D-SEM allows operators to choose SE or BSE images. The SE gives information of the surface morphology, but not of the geometric structure of the specimen. The BSE image is obtained in an RE mode. It is an elastic reflection with no energy loss. In other words, the image consists of electrons that reach the sample surface and are reflected back. The BSE signal contains both sample topography and composition as part of its information package. By using the four-quadrant divided detector, separating the shape effect and compositional effect is possible. The shape effect gives us the surface roughness information. Therefore, the use of a reflection electron image can offer precisely the profile analysis and, therefore, the surface roughness analyzer in an SEM uses RE and not SE.

The depth profile of the cavities formed by laser irradiation was examined by using the quantitative surface analyzing method of 3D-SEM and by direct observation after cross-sectioning the surface. The profiles obtained by noncontact surface analysis (Figs. 3 and 4) showed nearly the same outline as the direct cross-sectional observations (Figs. 1 and 2). The SEM profile analysis showed contours of melted globules on the Nd:YAG laser-irradiated dentin surface, but they were difficult to observe in the direct cross-sectional observation at the magnification used to view the whole cavity. SEM analysis by noncontact mode allows the depth profile to be measured on a μm scale that gives detailed analysis of the morphology. The Er:YAG laser made the deepest cavities in dentin and enamel. The dimension and spatial configuration of surface were reconstructed by 3D imaging from the orientation to be studied, and the details and surface roughness were easy to understand.

The lowest Ra value was for enamel and dentin after Nd:YAG and CO_2 laser irradiation, respectively. Although Er:YAG laser-irradiated dentin and enamel surfaces gave a large Ra due to deep cavity formation, the cavity surface was smooth (Fig. 5).

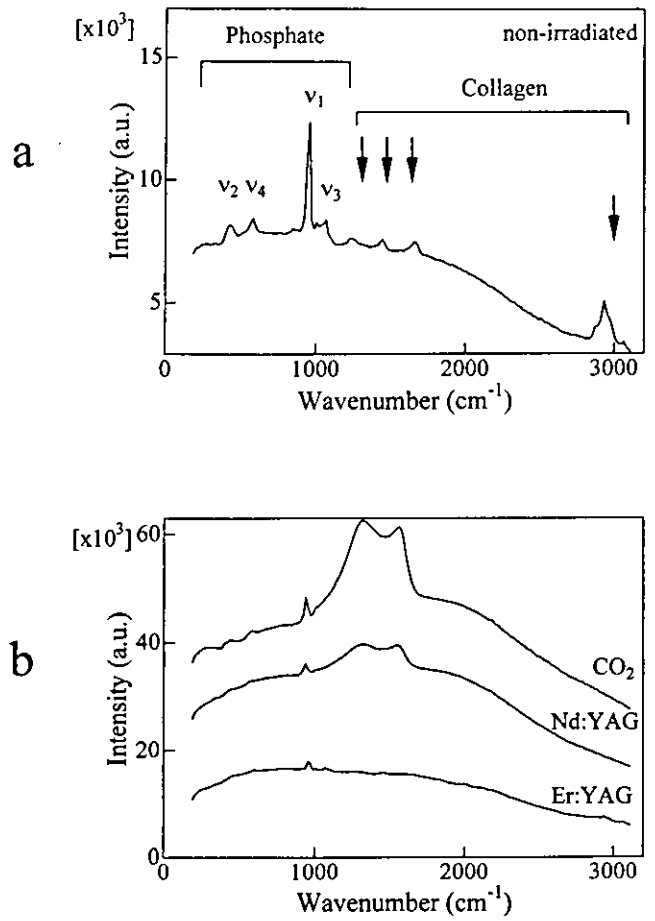

Figure 6. Raman spectra of (a) nonirradiated and (b) laser-irradiated dentin.

Raman Spectra

Raman bands at ν_2 (350–500 cm^{-1}), ν_4 (550–650 cm^{-1}), and ν_3 (1000–1130 cm^{-1}) were weaker than ν_1 (900–1000 cm^{-1}) band.

The background of Raman spectra was generally higher in the laser-irradiated dentin and enamel surfaces than in nonirradiated dentin and enamel. The background, mostly contributed by fluorescence, is lower as the binding is tighter.[11] Therefore, the high background in the laser-irradiated surface suggests a breakage of the crosslinking in the structure. The collagen peaks disappeared after Nd:YAG and CO_2 laser irradiation on the dentin surfaces and peaks attributed to amorphous carbon were observed. This finding suggests that laser irradiation heats instantly the tooth surface to a high temperature and carbonized the collagen and other proteins, resulting in a black cavity surface.

Effect of Three Different Laser Irradiations

Analysis of surfaces irradiated by three lasers showed different morphological characteristics due to different wavelengths of the lasers and consequently different tissue interaction. One primary factor that determines how effective a laser is to ablate tissue is the absorption of the laser at the wavelength at which it is emanating. The water extinction length is the length of the water column required to absorb 90% of the energy if the laser energy is presumed to be absorbed by a column of water. In the Er:YAG laser, the water extinction length is about 0.003 mm compared with CO_2, which is 0.03 mm. Thus the absorption of the Er:YAG in water is about 10 times greater than for CO_2. The absorption of the Er:YAG in water is 18.000–20.000 times greater than for the Nd:YAG laser.[12]

The impact of the laser beam into homogeneous tissue leads to the transformation of radiant energy into heat by absorption. The amount of energy absorbed depends on the absorption coefficient of each molecule in the tissue. The Nd:YAG laser at wavelength 1.06 μm has a lower absorption in water and also in hydroxyapatite than Er:YAG and the CO_2 laser. Due to this low absorption, the use of black ink is necessary to increase the absorption efficiency of the laser beam when the Nd:YAG laser is applied to the tooth. The absorption of water is the highest for Er:YAG at wavelength 2.94 μm, when the water molecules evaporated before the hydroxyapatite melted. The water vapor may cause an internal pressure resulting in microexplosions and consequent ablation of tissue. Although the CO_2 laser, wavelength 10.6

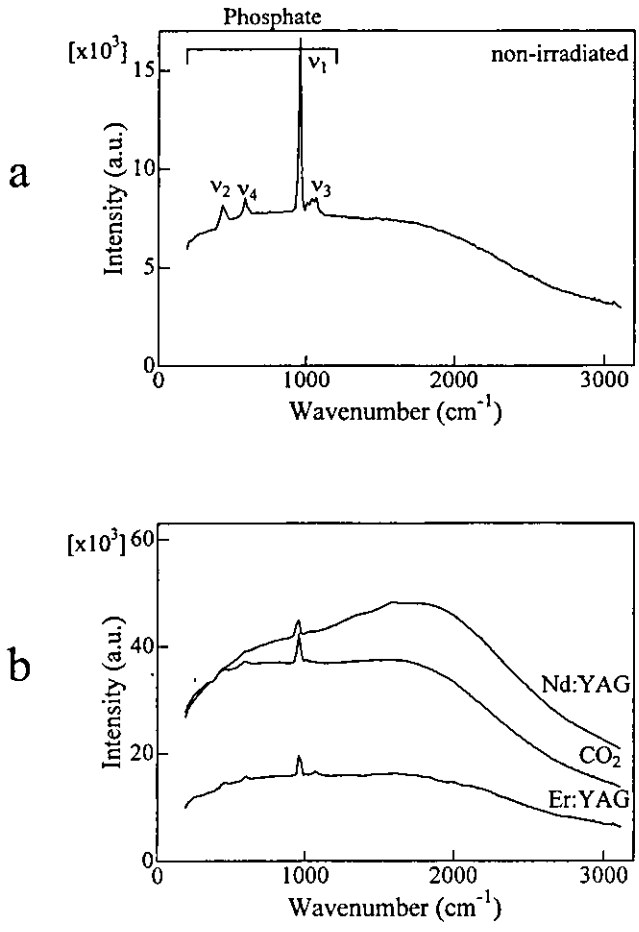

Figure 7. Raman spectra of (a) nonirradiated and (b) laser-irradiated enamel.

μm, has a high absorption rate by water, it is lower than the Er:YAG laser. The absorption of hydroxyapatite is higher than the absorption of water in the CO_2 laser. The absorption transforms the radiant energy into heat, resulting in an increase in temperature.[13] A high temperature ranges may cause cracks in the tooth structure. The mechanisms of hard tissue interaction produced by Nd:YAG and CO_2 lasers have been classified as photothermal interaction, and by the Er:YAG laser as photomechanical ablation of the tissue. These mechanisms produce different surfaces on enamel and dentin after each laser treatment.

Although other variables, such as pulse duration, pulse energy, number of pulses, repetition rate, and beam spot size influence the radiation effect,[14] the total energy is most directly related to the increase in cavity depth.[15] In this study, the total energy was greatest for Er:YAG (40 J) compared with Nd:YAG (0.6 J) and CO_2 lasers (3–4 J). Therefore, a suitable tooth ablation effect and formation of the deepest cavities observed in surfaces after Er:YAG laser irradiation depends on the higher absorption in water and higher total energy delivered.

The absorption of laser light varies depending on the nature of the biological tissue. The percentage of organic material in dentin is 20%, but in enamel this percentage decreases to 1–2%. This may explain the carbonization of dentin surfaces after Nd:YAG and CO_2 laser irradiation. Also, the higher percentage of organic material containing water in dentin may explain the deep cavity observed after Er:YAG irradiation in dentin compared with enamel.

The laser-irradiated surfaces had a generally rough surface compared with the nonirradiated surfaces. Thus, the laser-induced irregular tooth surface has the possibility to bond with composite resin by mechanical interlocking. However, in a Nd:YAG laser-irradiated dentin surface, such a bond strength may partly depend on the bond strength of the melted globules, which may not be so strong. Ariyaratnam et al.[16] also observed the same globule structure on dentin and showed that the bond strength after Nd:YAG laser irradiation is inferior to conventional dentin bonding. CO_2 laser-irradiated dentin had a smooth surface in this study. Other reports that used CO_2 laser alone have also found low levels of composite resin retention.[17] Its roughness may be enhanced by combination of acid etching pretreatment. The Nd:YAG and CO_2 laser-irradiated dentin showed signs of carbonization (black) affecting the appearance of tooth. Their application is suggested to be convenient for surface treatment, such as prevention of dental caries.[3]

However, the Er:YAG laser showed a surface with microirregularities without a smear layer, characteristics that promote micromechanical bonding of composite resin. Due to the high absorption of Er:YAG laser in water, and because intertubular dentin contains more water and has a lower mineral content than peritubular dentin, intertubular dentin is selectively ablated more than the peritubular dentin,[18] leaving protruding dentinal tubules with a cuff-like appearance. This may also contribute to an increase in the adhesive area. Therefore, Er:YAG laser showed suitable results for dental ablation and a favorable surface for mechanical bonding of a tooth with composite resin. The open dentinal tubules observed after Er:YAG laser irradiation may eliminate the need for acid-etching dentin as a pretreatment for composite bonding.

CONCLUSIONS

1. SEM and their respective surface roughness analyzers evaluate changes after laser irradiation on the dentin and enamel surfaces. Imaging and simultaneous quantitative analysis could provide an accurate description of the surface morphology.
2. An SEM profile by the noncontact mode nearly agreed with the direct observation by cross-section.
3. Raman spectroscopy showed that hydroxyapatite was partly decomposed, and that collagen was carbonized in dentin after Nd:YAG and CO_2 laser irradiation.
4. Er:YAG laser forms deep cavities without damage to the surrounding dentin, but Nd:YAG and CO_2 lasers are more suitable for surface treatment.

We would like to thank: Dr. Takaki Kumazawa, Dr. Yoji Kamiura, and the staff of Kumazawa Dental Clinic for the use of the CO_2 laser, Dr. Hiroshi Inoue for the use of Er:YAG laser, Dr. Yoshinobu Nodasaka and Mr. Toshi Sugawara of Hokkaido University for their kind help, and Hitachi High-Technologies Corporation for their 3D analysis using SEM.

REFERENCES

1. Maiman TH. Stimulated optical radiation in ruby. Nature 1960; 187:493–494.
2. Goldman L, Hornby P, Meyer R, Goldman B. Impact of the laser on dental caries. Nature 1964;203:417.
3. Yamamoto H, Sato K. Prevention of dental caries by acousto-optically Q-switched Nd:YAG laser irradiation. J Dent Res 1980;59:137.
4. Hibst R, Keller U. Experimental studies of the application of the Er:YAG laser on dental hard substances: I. Measurement of the ablation rate. Lasers Surg Med 1989;9:338–344.
5. Lobene RR, Bhussry BR, Fine S. Interaction of carbon dioxide laser radiation with enamel and dentin. J Dent Res 1968;47: 311–317.
6. Wigdor H, Abt E, Ashrafi S, Walsh JT, Jr. The effect of lasers on dental hard tissues. J Am Dent Assoc 1993;124:65–70.
7. Watari F. Compositional and morphological imaging of CO_2 laser irradiated human teeth by low vacuum SEM, confocal laser scanning microscopy and atomic force microscopy. J Mater Sci Mater Med 2001;12:189–194.
8. Spencer P, Cobb CM, McCollum MH, Wieliczka DM. The effects of CO_2 laser and Nd:YAG with and without water/air surface cooling on tooth root structure: Correlation between FTIR spectroscopy and histology. J Periodontal Res 1996;31: 453–462.
9. Ceballos L, Osorio R, Toledano M, Marshall GW. Microleakage of composite restorations after acid or Er-YAG laser cavity treatments. Dent Mater 2001;17:340–346.

10. Arcoria CJ, Lippas MG, Vitasek BA. Enamel surface roughness analysis after laser ablation and acid-etching. J Oral Rehabil 1993;20:213–224.
11. Workman JJ. Hand book of organic compounds. San Diego: A Harcourt Science and Techonology Co.; 2001. p. 339–349.
12. Paghdiwala AF. Er:YAG laser hard tissue effects. In: Moretti M, editor. Lasers in dentistry. Westford, MA: Penn Well Publishing Co; 1991. p 63–75.
13. Koort HJ, Frentzen M. Laser effects on dental hard tissues. In: Miserendino LJ, Pick RM, editors. Lasers in dentistry. Carol Stream, IL: Quintessence Publishing Co.; 1995 p 57–70.
14. McCormack SM, Fried D, Featherstone JD, Glena RE, Seka W. Scanning electron microscope observations of CO_2 laser effects on dental enamel. J Dent Res 1995;74:1702–1708.
15. McDonald A, Claffey N, Pearson G, Blau W, Setchell D. The effect of Nd:YAG pulse duration on dentine crater depth. J Dent 2001;29:43–53.
16. Ariyaratnam MT, Wilson MA, Blinkhorn AS. An analysis of surface roughness, surface morphology and composite/dentin bond strength of human dentin following the application of the Nd:YAG laser. Dent Mater 1999;15:223–228.
17. Whitters CJ, Strang R. Preliminary investigation of a novel carbon dioxide laser for applications in dentistry. Lasers Surg Med 2000;26:262–269.
18. Aoki A, Ishikawa I, Yamada T, Otsuki M, Watanabe H, Tagami J, Ando Y, Yamamoto H. Comparison between Er:YAG laser and conventional technique for root caries treatment in vitro. J Dent Res 1998;77:1404–1414.

原　著

歯科材料・器械 Vol. 23 No. 1　29－39（2004）

繊維強化プラスチック型審美矯正ワイヤーの湿潤環境下での機械的特性挙動

田中　聡[1]　亘理文夫[2]　飯田順一郎[1]

Change of Mechanical Properties of Esthetic Orthodontic Wire with Fiber Reinforced Plastic Structure in Wet Condition

Satoru TANAKA[1], Fumio WATARI[2] and Junichiro IIDA[1]

Keyword：Esthetic, Orthodontic wire, Acoustic emission, Silane coupling agent

FRP esthetic orthodontic wires were fabricated from CPSA glass fibers and Bis-GMA resin. The water absorption and change of mechanical properties were investigated in wet condition to simulate use in the oral cavity. As a result, the mechanical properties declined after water absorption for 3～6 hours. Decline of load and micro fracturing were found to be correlated by acoustic emission measurement during the stress relaxation test. In wet condition, AEs was 5～9 times higher than in dry condition. Silane-coupling suppressed the generation of micro fractures and decline of load. The modulus of longitudinal elasticity and load at 2 mm deflection in the flexural test was reduced by half and the permanent deflection increased after 24/hours under 2 mm fixed bending in wet condition. These changes were well represented using the energy required for 2 mm deflection as a single evaluation index. Silane-coupling agent decreased the exfoliation of glass fiber/matrix interface and suppressed the decline of mechanical properties.

キーワード：審美性，矯正用ワイヤー，アコースティックエミッション，シランカップリング剤

CPSA ガラス繊維と Bis－GMA レジンから繊維強化プラスチック型（FRP）審美矯正ワイヤーを調製し，口腔内使用の前段階として，湿潤条件下での吸水動態と機械的特性の経時的変化を調べた．吸水は約 3～6 時間で完了し，機械的特性は劣化した．AE 測定により応力緩和試験中の荷重低下と試料内部の微視的破壊を関連づけて観測できた．湿潤条件では乾燥条件の 5～9 倍の AE が発生したが，カップリング処理により荷重の低下速度が軽減され，AE の発生時期を延ばすことができた．定たわみ曲げ負荷後の 3 点曲げ試験から得られた縦弾性係数，2 mm たわみ時の荷重値は水中浸漬 24 時間後でほぼ半減し，永久変形量が増大した．これらの変化は 2 mm 変形させるのに要したエネルギーにより単一の指標として評価できた．ガラス繊維に対するカップリング処理はマトリックスレジンとの界面剥離を抑制し，機械的特性の劣化の軽減に寄与した．

緒　言

近年，歯科矯正治療において審美的要求が強く求められ，ブラケット[1,2]，結紮線[3～6]に関しては透明で耐久性のあるものが開発され臨床に広く使われている．しかし，矯正治療に必要不可欠のワイヤーに関しては金属製のものがほとんどであり，審美的に優れたワイヤーの臨床応用が望まれている．審美矯正ワイヤーの研究開発はこれまでにいくつか試みられてきたが，現在発表されているワイヤー[7～12]は臨床応用するには十分とは言えず

原稿受付　2003 年 9 月 22 日，受理　2003 年 10 月 7 日

[1]北海道大学大学院歯学研究科口腔機能学講座歯科矯正学分野（〒 060－8586　札幌市北区北 13 条西 7 丁目）

[2]北海道大学大学院歯学研究科口腔健康科学講座物性歯科理工学分野（〒 060－8586　札幌市北区北 13 条西 7 丁目）

[1]Section of Orthodontics, Department of Oral Functional Science, Division of Medical Science, Graduate School for Dentistry, Hokkaido University (Kita 13, Nishi 7, Kita-ku, Sapporo 060-8586)

[2]Section of Dental Materials and Engineering, Department of Oral Health Science, Division of Medical Science, Graduate School for Dentistry, Hokkaido University (Kita 13, Nishi 7, Kita-ku, Sapporo 060-8586)

普及には至っていないのが現状である．

筆者らが研究開発を進めているカルシウムとリン酸イオンを含み生体親和性に優れた $27.5CaO-16.6P_2O_5-31.2SiO_2-24.5Al_2O_3$（CPSA）系ガラス繊維[13~15]の無機材料と，マトリックスにレジン系有機材料を複合した繊維強化プラスチックス型審美性矯正ワイヤー（以下，FRP ワイヤー）は，透明性が高く審美的に優れ，これまでの 3 点曲げ試験などの基礎的研究から臨床応用に適する曲げ強さを有することが示されている[16~24]．しかし，アーチワイヤーは口腔内で長期使用されるため湿潤条件下での長期的な材料特性についても検討する必要がある．歯科充填材料や有床義歯用材料にも用いられているレジンには吸水性があることがすでに知られている．矯正用ワイヤーの様に臨床上変形させる必要がある場合にはその機械的特性にレジンの吸水性が大きく影響するものと思われ，その対策は早急に検討すべき課題である[25~27]．

本研究では，口腔内使用の前段階として，FRP ワイヤーの湿潤条件下における吸水動態を調べ，機械的特性の経時的変化を応力緩和試験，アコースティックエミッション（AE）測定，定たわみ曲げ試験を用いて解析することを目的とした．

材料および方法

1. FRP ワイヤー試料

図 1 に FRP ワイヤーの模式図を示す．ワイヤー成形に先立ちガラス繊維とマトリックスとの間の接着強さの向上を目的として，カップリング処理剤 KBM403（γ-グリシドキシプロピルトリメトキシシラン，信越シリコーン）を CPSA ガラス繊維（ユニチカグラスファイバー，直径約 20 μm）に使用した．マトリックスにはビスフェノール A-ジグリシジルメタクリレート（Bis-GMA，新中村化学）を用い，一方向配向型，円形断面の FRP ワイヤーを豊泉らが考案した光重合法[23]により作製した．以下，カップリング処理を施されたガラス繊維を用いた試験片を 403 ワイヤー，また比較のために，無処理のガラス繊維を用い作製した試験片を無処理ワイヤーと呼ぶことにする．本研究では繊維体積分率（以下，V_f）

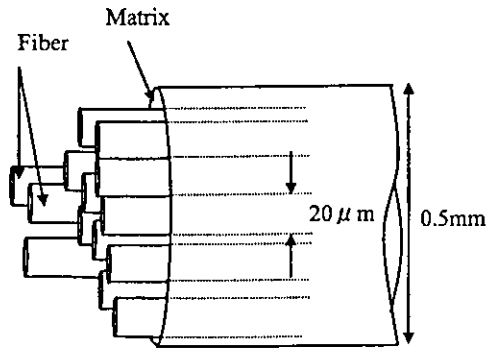

図 1 FRP ワイヤーの模式図

30%，直径 0.5 mm のワイヤーを長さ 30 mm に切りそろえたものをそれぞれ試料として用いた．

2. 吸水率の測定

1) 吸水試験

試験は無処理，403 と比較のためガラス繊維のまったく入っていないレジンのみのワイヤーをそれぞれ 4 本ずつ用いて行った．試験片をデシケーター中で恒量となるまで乾燥させ，37℃ の蒸留水に 3，6，12，24 時間浸漬した．水中から取出した後，乾燥した清潔なガーゼで水分を拭き，5 分間放置後に重量をミクロ分析天秤（AEM-5200，島津）にて秤量した．ガラス繊維の吸水は無視できるため，各 FRP ワイヤー重量からガラス繊維重量を差し引いた値をマトリックス部重量とし，下記の式より吸水率を求めた．

マトリックス部の吸水率 $= (m-m_0)/m_0 \times 100$ (%)

m：吸水後のマトリックス部の重量

m_0：乾燥恒量時のマトリックス部の重量

2) 吸水-乾燥試験

吸水と乾燥による FRP ワイヤーの機械的特性への影響を評価するために，吸水-乾燥試験を行った．試験は無処理ワイヤーと 403 ワイヤーについてそれぞれ 4 本ずつ行った．

全試験片を吸水の前にデシケーターで乾燥し恒量とした（m_0）．秤量は 37℃ 蒸留水中に 24 時間浸漬後（m_w），23℃ 湿度 50% 大気中で 1 時間乾燥後（m_{23}），100℃ の恒温槽で 1 時間乾燥後（m_{100}）にも行い，いずれも吸水試験と同様に各 FRP ワイヤー重量からガラス繊維重量を差し引いた値をマトリックス部の重量とし，以下の式を用いて吸水率を求めた．

浸漬，乾燥後の吸水率 $= (m_T-m_0)/m_0 \times 100$ (%)

T：w（浸漬後），23℃，100℃

3. 機械的特性試験

1) 3 点曲げ試験

口腔内は飲食により温度が大きく変化するだけでなく，様々な物質が存在する湿潤環境でもある．始めに浸漬による機械的特性の低下は水特有に起こるものなのか，もしくは有機溶媒のような溶解性のある他の液体でも起こるのか調べた．37℃ 純水中および浸透探傷試験などに使用する有機溶媒（スーパーグロー蛍光浸透液 OD-2800 Ⅳ，マークテック社製，アルキルベンゼン 30wt%，フタル酸エチルヘキシル 49wt%，ポリノニルフェニルエーテル 12wt%）中に，無処理ワイヤーを 4 本ずつ 24 時間浸漬したものについてインストロン万能試験機（Model 4204）を用いて支点間距離 14 mm，支点直径 3 mm，クロスヘッドスピード 1 mm/min，たわみ 0 から 4 mm の間で 1 往復の 3 点曲げ試験を行った．

次に吸水-乾燥試験を行った 3 つのグループと浸漬前の試料についても同様の条件で試験を行い，2 mm 変形エネルギーを求めた．2 mm 変形エネルギーは得られた荷重-たわみ曲線のたわみ 2 mm までの曲線に囲まれる

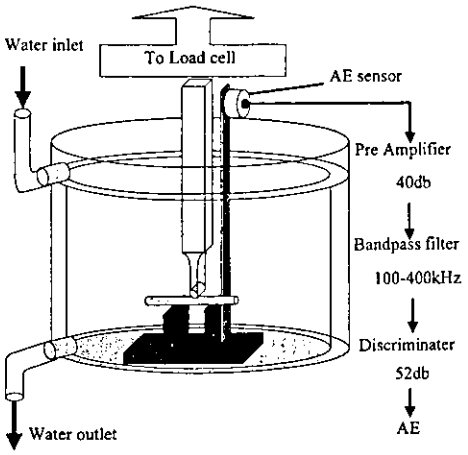

図2　応力緩和試験および AE 測定の模式図

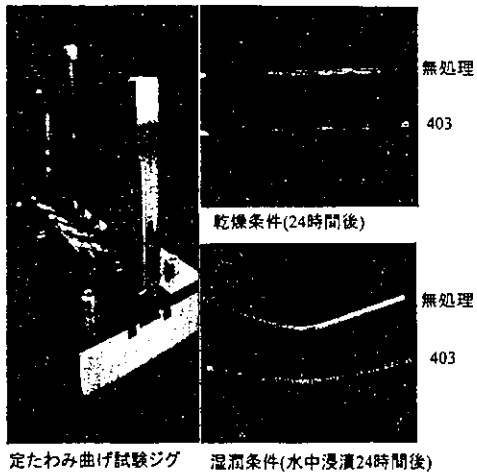

図3　定たわみ曲げ試験ジグと試験直後のワイヤーの変形

面積として求めた．データ処理には専用の付属コンピューター（Dimension XPS T450，DELL）にデータをサンプリングレート 20 point/sec でリアルタイムに読み込み，演算処理を行った．

2)　応力緩和試験

機械的特性の負荷時間による変化を調べるために 403 ワイヤーおよび無処理ワイヤーについて，乾燥条件（大気中）および湿潤条件（水中）での応力緩和試験を各条件につきそれぞれ1本ずつ行った．Imai らが製作した水槽型試験ジグ（図2）[26] とインストロン万能試験機を用い，室温 23℃，湿度 50% の乾燥条件下，または 37℃ 水中の湿潤条件下で支点間距離 14 mm，支点直径 3 mm，クロスヘッドスピード 1 mm/min で，たわみ 2 mm の曲げ変形を負荷後 24 時間保持し，記録した応力の最大荷重値に対する比率を求め，これを荷重保持率とし評価に用いた．

3)　アコースティックエミッション（AE）測定

応力緩和試験における微視的な破壊を検出するために AE を計測した．試験片の塑性変形，クラックの発生などによって放出された AE は，図2に示す曲げ試験機の台座に伝播し，次に台座に取り付けられたウェーブガイドによって AE センサーに伝達される．ここで検出された AE はプリアンプで 40db に増幅され，バンドパスフィルターを経て閾値をこえた信号を AE とした．なお AE を処理して得られる情報として計数，振幅，波形，立ち上がり時間，持続時間などがある．本研究では劣化の程度を推定するために計数を用いた．通常，計数は閾値を超えた AE 発生数を計測する．この事象計測法では振幅の大きい AE も小さい AE も同じ扱いになる．そこで，振幅による重み付けをつけるために，閾値を越えた波のサイクル数を全部数えるリングダウン法[28] を計測法として用いた．また評価には AE 計数と，それを積算した AE 累積数を用いた．

4)　定たわみ曲げ試験

一度曲げ変形を付与されたワイヤーの機械的特性を調

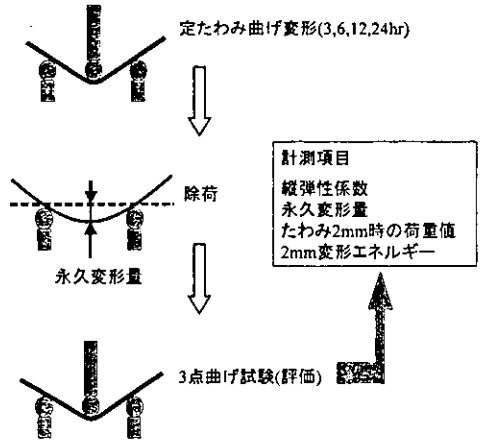

図4　定たわみ曲げ試験の模式図

べるために 403 ワイヤー，無処理ワイヤーをそれぞれ7本ずつ用いて定たわみ曲げ試験を行った．図3左に自作した定たわみ曲げ試験ジグを示す．なお右側の写真は，定たわみ曲げ試験後の試験片の状態を示す．これに関しては後述する．このジグは3点曲げ試験機と同じ支点間距離，支点直径を持ち，複数の試験片に一定のたわみを同時に与えることができる．ジグ上に置かれた試験片の中央部に速度 1 mm/min で圧子をたわみ 2 mm まで押しつけた後，所定の時間（3，6，12，24 時間）保持した．湿潤条件ではジグごと 37℃ の純水恒温槽に浸漬した．図4に定たわみ曲げ試験の模式図を示す．試験は定たわみ曲げ変形を付与する第1段階と，曲げ変形の解放後，変形の回復が収まるのを待って3点曲げ試験を行い評価する第2段階とからなる．

3点曲げにより得られた荷重－たわみ曲線から永久変形量，緩弾性係数，2 mm 荷重値，2 mm 変形エネルギーを求めた．ここでは変形のないワイヤーとロードセルが触れる位置を0とし，定たわみ曲げ変形後のワイ

ヤーとロードセルが触れる位置を永久変形量とした．縦弾性係数（E）は荷重がかかり始めた位置からたわみが0.2 mmでの荷重値を求め，以下の式より算出した[29]．

$E=4pl^3/3\ \delta\ \pi\ d^4$

l：支点間距離，d：試料直径，δ：たわみ（今回は0.2を使用），p：荷重値

また，変形のないワイヤーとロードセルが触れる位置を0とし，たわみが2 mmの時点での荷重値を2 mm荷重値，荷重－たわみ曲線のたわみ2 mmまでの曲線に囲まれる面積を2 mm変形エネルギーとして求めた．

4. 統計処理

吸水試験では吸水率，吸水－乾燥試験では吸水率と2 mm変形エネルギー，定たわみ曲げ試験では縦弾性係数，2 mm荷重値，永久変形量および2 mm変形エネルギーの平均値と標準偏差を求め，t検定を行い，試験条件間およびカップリング処理の有無について有意差を算出した．

結　　果

1. 3点曲げ試験

図5は無処理ワイヤーを37℃の水ならびに有機溶媒中に24時間浸漬後に3点曲げを行った結果である．有機溶媒に浸漬したワイヤーの荷重－たわみ曲線は，浸漬前のものとほとんど変わらないが，たわみ2.5 mmを超えた付近で破折が起こり始めた．一方，水中に24時間浸漬したものは浸漬前と比べると弾性が明らかに低下しているが，たわみ4 mmまで明確な破断は見られなかった．

2. 吸水試験

図6に吸水率の浸漬時間による変化を示す．いずれの試験片も3～6時間で吸水をほぼ完了しており，その後はわずかしか上昇しない．無処理ワイヤーの吸水率は浸漬6時間後でのみ403ワイヤーに比べ有意に高かった（$p<0.05$）．またレジンのみでできているワイヤーの吸水率は約3.6%で，無処理ワイヤーより有意に低かった（$p<0.01$）．

3. 吸水－乾燥試験

1) 吸水率

図7に吸水－乾燥試験における各条件での吸水率を示す．浸漬直後の吸水率は403ワイヤーも無処理ワイヤーも約4%と近い結果が得られ，23℃1時間乾燥すると約2%，100℃1時間乾燥すると元よりも軽くなり約－0.6%となった．各条件間で有意差が認められたが（$p<0.01$），無処理ワイヤーと403ワイヤー間には有意差は認められなかった（$p>0.05$）．

2) 荷重－たわみ曲線

(1) 無処理ワイヤー

図8に無処理ワイヤーの荷重－たわみ曲線を示す．浸漬直後（a）の勾配は浸漬前（0）に比べて明らかに小さいが，たわみが4 mmに達しても破折しなかった．23℃で1時間乾燥した（b）は（a）に比べ勾配が大きいが，

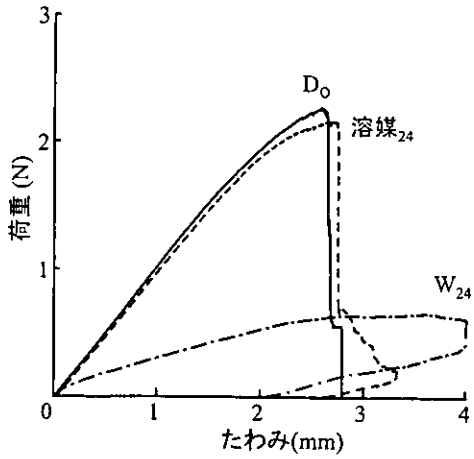

図5　液中浸漬（37℃ 24時間）後の荷重－たわみ曲線（無処理）
溶媒$_{24}$：有機溶媒，W_{24}：水中，D_0：浸漬前

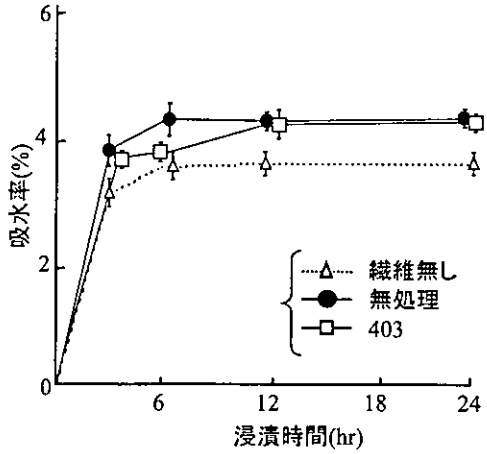

図6　吸水率の浸漬時間による変化

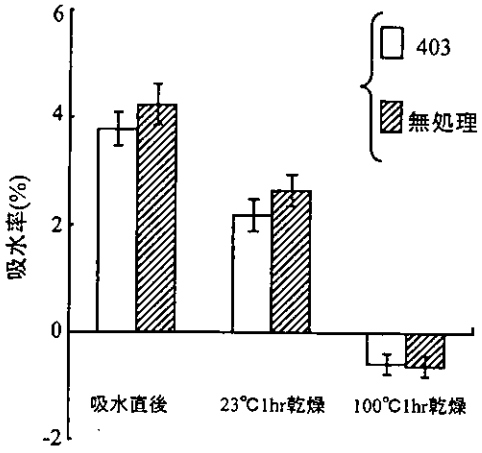

図7　吸水率の乾燥条件による変化

3 mmを越えた辺りから鋸歯状の荷重低下を示し局所的な破壊が開始していた．100℃で1時間乾燥した（c）は浸漬前の（0）とほぼ同じ程度の勾配になったが，やや早い段階（たわみ約2 mm）で鋸歯状の荷重低下が見ら